AMERICAN SOCIETY FOR MICROBIOLOGY | mBio

Check for updates

| Virology | Research Article

Multifaceted roles for STAT3 in gammaherpesvirus latency revealed through *in vivo* B cell knockout models

Chad H. Hogan,[1,2] Shana M. Owens,[3] Glennys V. Reynoso,[4] Yifei Liao,[5] Thomas J. Meyer,[6,7] Monika A. Zelazowska,[8] Bin Liu,[8] Xiaofan Li,[2] Anna K. Grosskopf,[2] Camille Khairallah,[9] Varvara Kirillov,[9] Nancy C. Reich,[9] Brian S. Sheridan,[9] Kevin M. McBride,[8] Benjamin E. Gewurz,[5,10,11,12] Heather D. Hickman,[4] J. Craig Forrest,[3] Laurie T. Krug[2,9]

AUTHOR AFFILIATIONS See affiliation list on p. 24.

ABSTRACT Cancers associated with the oncogenic gammaherpesviruses, Epstein-Barr virus and Kaposi sarcoma herpesvirus, are notable for their constitutive activation of the transcription factor signal transducer and activator of transcription 3 (STAT3). To better understand the role of STAT3 during gammaherpesvirus latency and the B cell response to infection, we used the model pathogen murine gammaherpesvirus 68 (MHV68). Genetic deletion of STAT3 in B cells of *CD19*$^{cre/+}$*Stat3*$^{f/f}$ mice reduced peak MHV68 latency approximately sevenfold. However, infected *CD19*$^{cre/+}$*Stat3*$^{f/f}$ mice exhibited disordered germinal centers and heightened virus-specific CD8 T cell responses compared to wild-type (WT) littermates. To circumvent the systemic immune alterations observed in the B cell-STAT3 knockout mice and more directly evaluate intrinsic roles for STAT3, we generated mixed bone marrow chimeric mice consisting of WT and STAT3 knockout B cells. We discovered a dramatic reduction in latency in STAT3 knockout B cells compared to their WT B cell counterparts in the same lymphoid organ. RNA sequencing of sorted germinal center B cells revealed that MHV68 infection shifts the gene signature toward proliferation and away from type I and type II IFN responses. Loss of STAT3 largely reversed the virus-driven transcriptional shift without impacting the viral gene expression program. STAT3 promoted B cell processes of the germinal center, including IL-21-stimulated downregulation of surface CD23 on B cells infected with MHV68 or EBV. Together, our data provide mechanistic insights into the role of STAT3 as a latency determinant in B cells for oncogenic gammaherpesviruses.

IMPORTANCE There are no directed therapies to the latency program of the human gammaherpesviruses, Epstein-Barr virus and Kaposi sarcoma herpesvirus. Activated host factor signal transducer and activator of transcription 3 (STAT3) is a hallmark of cancers caused by these viruses. We applied the murine gammaherpesvirus pathogen system to explore STAT3 function upon primary B cell infection in the host. Since STAT3 deletion in all CD19+ B cells of infected mice led to altered B and T cell responses, we generated chimeric mice with both normal and STAT3-deleted B cells. B cells lacking STAT3 failed to support virus latency compared to normal B cells from the same infected animal. Loss of STAT3 impaired B cell proliferation and differentiation and led to a striking upregulation of interferon-stimulated genes. These findings expand our understanding of STAT3-dependent processes that are key to its function as a pro-viral latency determinant for oncogenic gammaherpesviruses in B cells and may provide novel therapeutic targets.

KEYWORDS gammaherpesvirus, human herpesviruses, Kaposi sarcoma-associated herpesvirus, latent infection, host-pathogen interactions, STAT transcription factors

The human gammaherpesviruses (GHVs), Epstein-Barr virus (EBV, human herpesvirus 4) and Kaposi sarcoma herpesvirus (KSHV, human herpesvirus 8), are the etiologic

Editor Thomas Shenk, Princeton University, Princeton, New Jersey, USA

Address correspondence to Laurie T. Krug, laurie.krug@nih.gov.

The authors declare no conflict of interest.

See the funding table on p. 25.

Received 3 November 2023
Accepted 14 November 2023
Published 3 January 2024

agents of numerous lymphomas and carcinomas that are a significant clinical burden to immune-compromised individuals, including people living with HIV. Even in immune-competent individuals, infection with EBV may manifest as infectious mononucleosis and increase the risk for the development of multiple sclerosis, an autoimmune disorder involving inflammation and neurodegeneration in the central nervous system (1). B cells are a long-term reservoir for GHV, and these viruses usurp host processes such as proliferation and differentiation to facilitate chronic infection (2–5). The identification of host factors that support latency and facilitate the emergence of GHV-driven malignancies is paramount as there are currently no treatments that directly target the latent phase of infection.

A hallmark of GHV infection and GHV cancers is the rapid and persistent activation of signal transducer and activator of transcription 3 (STAT3) (6). STAT3 is a master regulator of multiple cellular processes such as proliferation, apoptosis, and metastasis (7, 8). Constitutive STAT3 activation is reported in multiple human cancers (9, 10). Cytokines are potent activators of STAT3 in both cancer and immune cells. For instance, IL-6 induces the expression of STAT3-target genes responsible for proliferation and survival supporting tumorigenesis, while IL-10 reduces immune cell function and inflammation in some contexts (11, 12). The human GHVs use diverse strategies to promote STAT3 activation (6). EBV transmembrane protein LMP1 activates NF-κB through recruitment of cytoplasmic signaling adaptors leading to IL-6-driven STAT3 activation and cell survival (13, 14). EBV LMP2A activates STAT3 through multiple host factors to promote proliferation and survival (15, 16). The viral homologs of host cytokines, EBV vIL-10 and KSHV vIL-6, and the KSHV vGPCR also activate STAT3 (17–21).

Due to their narrow host range, the study of EBV and KSHV is largely restricted to cell culture and humanized mouse models. For that reason, murid herpesvirus 4, more commonly known as murine gammaherpesvirus 68 (MHV68), is used as a model pathogen. MHV68 is colinear with KSHV, encoding 64 direct homologs, establishes long-term latency in memory B cells, and induces lymphoproliferation in immunosuppressed mice (5). The infection of mice with MHV68 is a genetically tractable system to study virus-host interactions in specific cell types during the acute or chronic phase of infection in a natural host. Viral and host factors such as NF-κB signaling pathways support the establishment and latency in B cell compartments (5, 22–27).

The interplay of viral and host factors aids in the establishment and expansion of GHV latency, taking particular advantage of B cell processes occurring during the germinal center (GC) reaction. The GC is the site within secondary lymphoid tissues where B cells undergo maturation and differentiation processes including somatic hypermutation and class switch recombination, leading to the production of high-affinity and long-lived memory B cell and plasma cell subsets (28, 29). GHVs both engage and circumvent the GC B cell selection process to promote access to the memory B cell long-term latency reservoir for EBV and likely for KSHV (30–33); events that transpire in the GC may contribute to B cell lymphomas with post-germinal center signatures (34–36). At the peak of latency establishment ~16 days post-infection (dpi), MHV68 is predominantly found in B cells bearing GC markers (22). T follicular helper cell production of IL-21 is required to support MHV68 latency establishment in GC B cells (24), while Blimp-1 is required to access the post-GC plasma cell compartment that is a source of virus reactivation (37). The MHV68 viral M2 protein promotes host IL-10 production through the nuclear factor of activated T cells (NFAT) pathway, promoting proliferation and differentiation, driving B cells to a plasmablast-like phenotype *in vivo* (38–40). MHV68 RTA protein encoded by ORF50 acts synergistically with STAT3 to increase transcriptional activity in response to IL-6 (41). Given the critical role of STAT3-activating cytokines IL-10 and IL-21 in MHV68 infection (24, 38) and the evolutionary investment by the GHVs to subvert STAT3 signaling, we sought to further dissect the role of STAT3 in GHV latency establishment *in vivo*.

We previously used a mouse model in which STAT3 is ablated specifically in the CD19+ B cell compartment to discover that STAT3 is a crucial host determinant of MHV68

latency establishment in B cells *in vivo* (42). In the present study, we more closely examined virus latency in GC subsets and virus-specific adaptive immune responses in two independent strains of *CD19*$^{cre/+}$*Stat3*$^{f/f}$ mice to eliminate possible strain variation. We identified disordered GC architecture in B cell-specific STAT3 knockout (KO) mice, along with reduced virus-specific antibody production, concomitant with a heightened CD8+ T cell response. This aberrant immune response in the absence of STAT3 signaling in B cells led us to use a mixed bone marrow (BM) chimera approach wherein mice are reconstituted with hematopoietic cells from wild-type (WT) and B cell-specific STAT3 KO mice. Infection of mixed bone marrow chimeric mice revealed that B cells lacking STAT3 could not compete with their wild-type counterparts to support GHV latency. To gain mechanistic insight into the transcriptional consequences of STAT3 loss, we sorted STAT3 WT and KO GC B cells, with or without infection, and quantified gene expression profiles with RNA sequencing. We identified numerous host gene pathways altered by STAT3 that intersect processes of B cell biology and host response to infection.

RESULTS

Loss of STAT3 in B cells disrupts gammaherpesvirus latency and leads to abnormal GC structure

Mice with *loxP*-flanked exons of *Stat3* (*Stat3*$^{f/f}$) that are crossed with mice expressing Cre recombinase under the control of the endogenous *CD19* promoter exhibit loss of STAT3 only in CD19+ B cells (43). Our lab previously reported that the conditional knockout of STAT3 in B cells led to a severe defect in the establishment of MHV68 latency in the spleens of mice after intranasal or intraperitoneal (IP) infection (42). In this study, we compared MHV68 latency in two strains of B cell-specific STAT3 knockout mice that differ by the location of *loxP* sites that flank exons of the *Stat3* gene (Fig. 1A) (44, 45). Consistent with our previous report for the *CD19*$^{cre/+}$*Stat3*$^{f/f}$-1 mice, the CD19+ B cell population of the *CD19*$^{cre/+}$*Stat3*$^{f/f}$-2 mice lacked detectable levels of STAT3 protein by immunoblot (Fig. 1A). For brevity, *Stat3*$^{f/f}$ mice will be referred to as WT mice, and their littermate *CD19*$^{cre/+}$*Stat3*$^{f/f}$ mice will be referred to as B cell-STAT3 KO mice. STAT3 tyrosine 705 (Y705) phosphorylation is the classical indicator of STAT3 activation, and this activation has been demonstrated in response to human GHV infection in cell culture with endothelial, dendritic, and B cell models (46–49). We used intracellular flow cytometry staining of splenocytes from infected mice to reveal a higher level of STAT3-Y705 phosphorylation in B cells from the spleens of infected WT mice compared to the infected littermate B cell-STAT3 KO mice (Fig. 1B).

We previously reported that the loss of STAT3 in B cells did not affect acute replication of MHV68 in the lungs of mice after intranasal infection but led to such a profound defect in latency establishment in the spleen that infected B cells were barely at the limit of detection (42). Here, we aimed to investigate the phenotype of infected B cells in the absence of STAT3, requiring us to use the more permissive IP route of infection to enable sufficient infected cells for analysis. At 16 dpi, the peak of the early phase of splenic latency, infected mice exhibit an enlargement of the spleen that follows colonization of that tissue with MHV68 (5). Spleens from both strains of B cell-STAT3 KO mice were significantly reduced in mass upon infection compared to the fourfold increase in mass observed upon infection of WT animals (Fig. 1C). The MHV68-H2bYFP recombinant virus utilizes a CMV immediate early promoter, driving constitutive expression of a histone 2b-YFP fusion protein and enabling direct analysis of infected cells (22). Consistent with the defect in splenomegaly, the frequency of B cells that expressed the YFP viral reporter gene determined by flow cytometry was reduced by three- and twofold in the spleens of the strain 1 and strain 2 B cell-STAT3 KO mice, respectively, when compared to their WT littermates (Fig. 1D). This defect in latency was confirmed by a limiting dilution nested PCR assay to quantify the frequency of B cells harboring the viral genome. A 6.6-fold defect in the frequency of infected splenocytes that harbor the MHV68 genome was observed for *CD19*$^{cre/+}$*Stat3*$^{f/f}$-2 mice (1 positive event per 1,688 cells, 1/1,688) compared to *Stat3*$^{f/f}$-2 WT mice (1/256) (Fig. 1E). Furthermore, in a limiting dilution reactivation

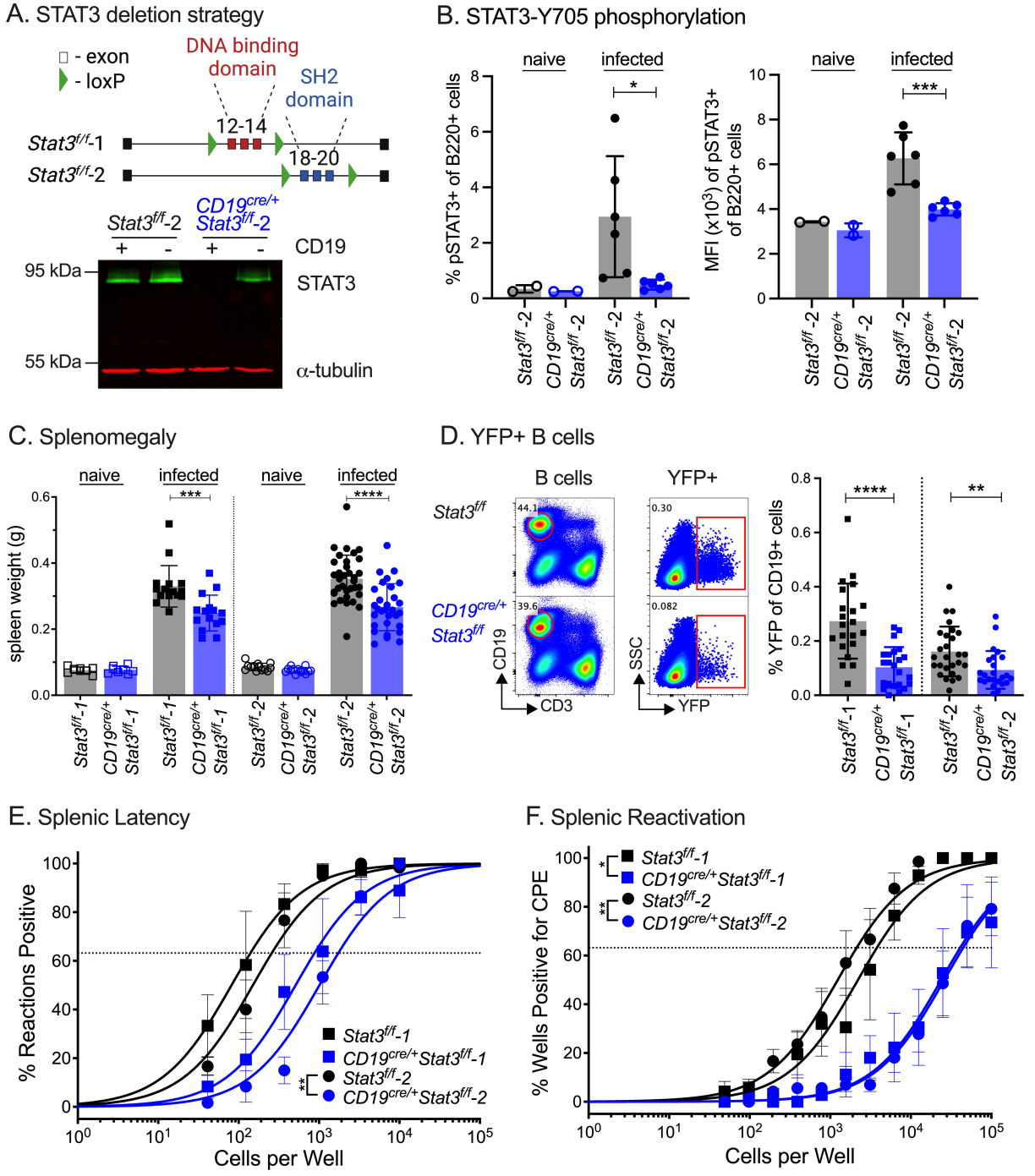

FIG 1 STAT3 is necessary for the efficient establishment of latency in B cells of infected mice. (A) Schematic of *loxP*-flanked exons of the *Stat3* locus in two strains of *CD19*$^{cre/+}$*Stat3*$^{f/f}$ mice. Immunoblot confirmation of STAT3 loss in CD19+ B cells of *CD19*$^{cre/+}$*Stat3*$^{f/f}$-2 mice, but not CD19- non-B cells, as previously described for *CD19*$^{cre/+}$*Stat3*$^{f/f}$-1 mice (42). (B–F) *Stat3*$^{f/f}$ and *CD19*$^{cre/+}$*Stat3*$^{f/f}$ mice were infected with 1,000 PFU MHV68-H2bYFP by intraperitoneal inoculation and evaluated at 16 days post-infection. (B) Intracellular staining of STAT3-Y705 phosphorylation in B220^{+} B cells of naive or infected mice evaluated as frequency of pSTAT3+ B220+ cells (left panel) and mean fluorescence intensity (MFI, right panel). (C) Weights of spleens from naive or infected mice. (D) Flow cytometry gating strategy (left panel) of infected (YFP+) B cells (CD19^{+}CD3^{-}) and enumeration of frequencies in each strain of mice (right panel). For B–D, each symbol represents an individual mouse; bars represent mean ± SD. Data shown represent two to three independent experiments performed with three to seven mice per infected group and one to two mice for naive groups. (E) Single-cell suspensions of spleen cells were serially diluted, and the frequencies of cells harboring an MHV68 genome were determined using a limiting dilution PCR analysis. (F) Reactivation frequencies were determined by *ex vivo* plating of serially diluted cells on an indicator monolayer. Cytopathic effect (CPE) was scored 3 weeks post-plating. For the limiting dilution analyses (E, F), curve fit lines were determined

(Continued on next page)

FIG 1 (Continued)

by non-linear regression analysis; frequency values were determined by Poisson analysis, indicated by the dashed line. Symbols represent the mean ± SEM. Statistical significance was evaluated by two-tailed unpaired *t* test (B, C, D) or paired *t* test of the calculated frequencies (E, F). *$P < 0.05$; **$P < 0.01$; ***$P < 0.001$; ****$P < 0.0001$.

assay, a 10- and 20-fold defect in spontaneous reactivation was observed upon explant of splenocytes from strain 1 and strain 2 of B cell-STAT3 KO mice compared to their WT counterparts, respectively (Fig. 1F). This reactivation defect largely mirrors the differences in latency at 16 dpi. A time course analysis of YFP+ B cells spanning 10–15 dpi was performed in strain 2 B cell-STAT3 KO mice. The absence of STAT3 led to a trend in decreased splenomegaly and a significant reduction in B cell infection as early as 12 dpi compared to WT counterparts (Fig. S1). These results confirm the importance of STAT3 in B cells for the efficient establishment of MHV68 latency in two strains of *CD19*$^{cre/+}$*Stat3*$^{f/f}$ mice.

The GC reaction represents an anatomical structure within secondary lymphoid organs in which activated B cells undergo clonal selection and affinity maturation. Additionally, most MHV68-infected cells express GC B cell markers at the peak of latency (22). Thus, we further examined GC B cell infection and latency in B cell-STAT3 KO animals. Compared to WT littermates, B cell-STAT3 KO exhibited increased frequencies of GC B cells (defined here as GL7+CD95^{hi} of CD19+ cells) at 16 dpi (Fig. 2A). Although there was a reduction in the frequency of YFP+ B cells in B cell-STAT3 KO mice (Fig. 1D), we observed no significant difference in the frequency of YFP+ cells that displayed a GC phenotype (Fig. 2B). GC B cells can be roughly subdivided into rapidly proliferating centroblasts (CXCR4+CD86–) that are found in the dark zone and mature, non-dividing centrocytes (CXCR4– CD86+) in the light zone. By flow cytometry, infected WT mice had a 2:1 ratio of respective centroblast:centrocyte populations (Fig. 2C). However, in the absence of B cell-STAT3, we observed decreased frequencies of centroblasts in both GC B cells and YFP+ GC B cell populations that resulted in a ratio closer to 1:1 (Fig. 2C).

To further explore the increase in GC B cells of infected mice lacking B cell-STAT3, we examined GC architecture in the spleens by immunofluorescence (Fig. 2D). MHV68 infection of WT mice has previously been shown to result in the formation of visible, compact GCs within the splenic follicles (22). Interestingly, the B cell follicles appeared smaller and more diffuse in B cell-STAT3 KO mice than in WT spleens, even in uninfected animals. Upon infection, GC B cells did not remain in characteristic compact foci in B cell-STAT3 KO mice, instead appearing dispersed throughout the follicle and overlapping extensively with the follicular dendritic cell (FDC) network. In both WT and B cell-STAT3 KO mice, most of the YFP+ cells also expressed the GC marker GL7. These data indicate that STAT3-KO in B cells alone led to a significantly altered splenic architecture.

B cells typically exit the GC as class-switched, long-lived memory B cells or antibody-secreting plasma cells. STAT3 coordinates the upregulation of *Prdm1,* encoding Blimp-1, a master regulator of B cell differentiation into plasma cells in response to IL-21 (50, 51). Plasma cells are a source of MHV68 reactivation in the spleen (52). Therefore, we examined plasma cell frequency and infection in the B cell-STAT3 KO mice (Fig. 2E). The frequency of B220^{lo}CD138+ plasma cells between WT and B cell-STAT3 KO mice was similar (Fig. 2E), but we observed a marked reduction (>50%) in YFP+ B cells with a plasma cell phenotype in the B cell-STAT3 KO mice (Fig. 2F). Together, the increase in GC cells, the altered GC structure, and decrease in YFP+ plasma cells clearly indicate that broad GC defects occur in the absence of B cell-STAT3. Collectively, this deeper analysis of two strains of B cell-STAT3 KO mice confirmed the requirement for STAT3 to promote B cell latency and revealed shifts in B cell subsets of the GC at 16 dpi. Because we observed similar latency and immune responses in both strains of mutant STAT3 mice, we proceeded with *CD19*$^{cre/+}$*Stat3*$^{f/f}$-strain 2 mice for the remainder of the study.

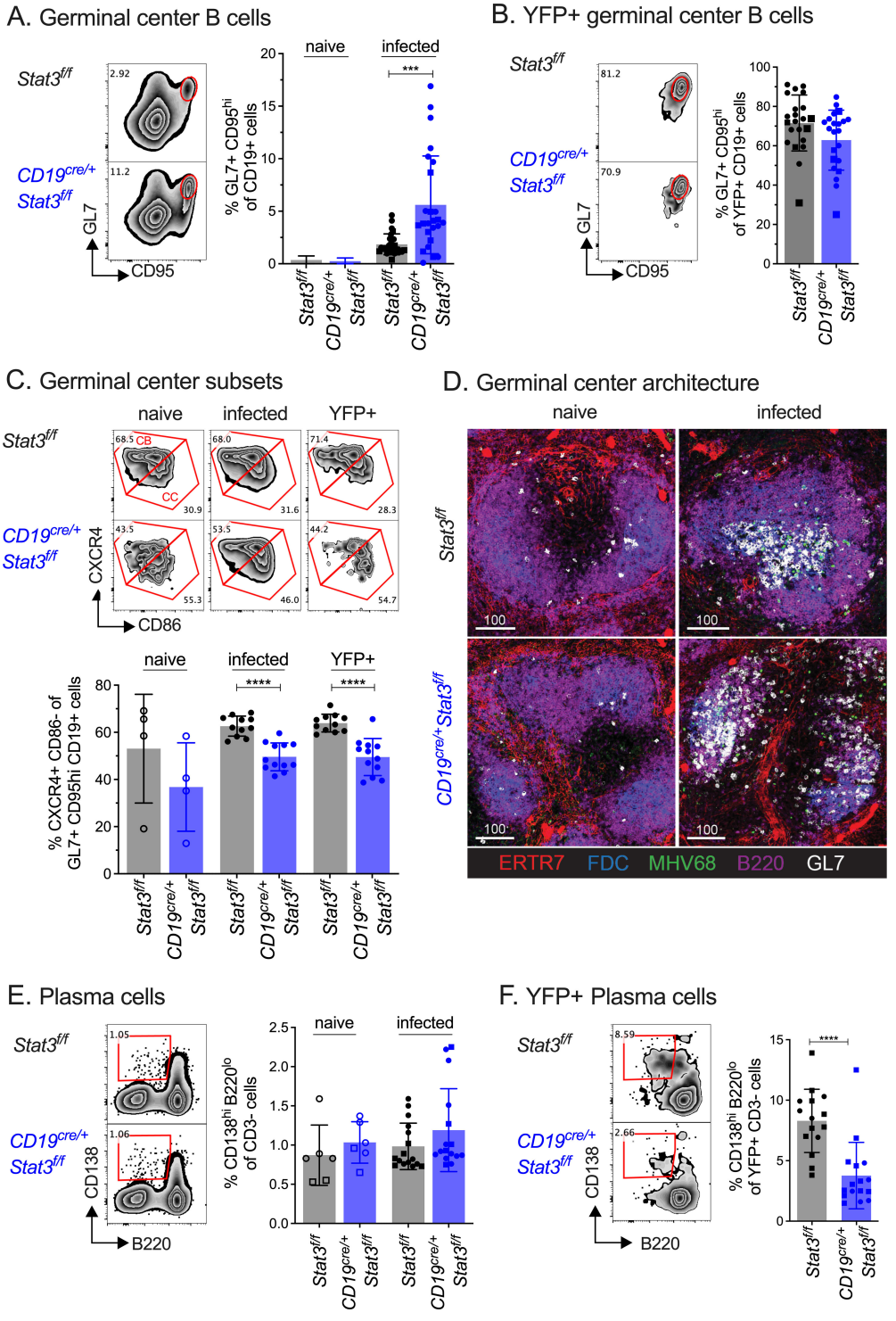

FIG 2 STAT3 loss in B cells leads to an aberrant germinal center response upon infection. *Stat3*$^{f/f}$ (WT) and *CD19*$^{cre/+}$*Stat3*$^{f/f}$ (B cell-STAT3 KO) mice were infected with 1,000 PFU MHV68-H2bYFP by intraperitoneal inoculation and evaluated at 16 dpi. (A) Flow cytometry gating strategy (left panel) and quantitation (right panel) of the frequencies of GC B cells (GL7+ CD95+ of CD19+ CD3−). (B) Flow cytometry gating strategy (left panel) and quantitation (right panel) of the frequencies of infected YFP+ cells bearing GC markers. (C) Flow cytometry gating strategy (upper panel) of dark zone centroblasts (CXCR4+ CD86−) and light zone centrocytes (CXCR4− CD86+) as a frequency of GC B cells from naive or infected mice, and infected YFP+ B cells from infected mice. Quantitation of the frequencies of centroblasts of GC B cells from naive or infected mice, and infected YFP+ B cells (lower panel). (D) Confocal microscopy of frozen spleen sections from naive mice (left panels) or infected mice

(Continued on next page)

FIG 2 (Continued)

(right panels) with STAT3 (*Stat3*$^{f/f}$-2, top panels) or without B cell STAT3 (*CD19*$^{cre/+}$*Stat3* $^{/f}$-2 mice, bottom panels) at 16 dpi to identify stromal cells (ERTR7, red), follicular dendritic cells (FDCs, blue), B220+ B cells (magenta), GC B cells (GL7, white), and MHV68-H2bYFP infection (green). Scale bars = microns. (E) Flow cytometry gating strategy (left panel) and quantitation (right panel) of the frequencies of plasma cells (CD138^{hi}B220^{lo} gated on CD3−). (F) Flow cytometry gating strategy (left panel) and quantitation (right panel) of the frequencies of infected YFP+ cells with plasma cell markers. Data shown represent the mean ± SD of two to three independent experiments performed with four to seven mice per infected group and one to two mice for naive groups. Each symbol represents an individual mouse. Square symbols represent *CD19*$^{cre/+}$*Stat3*$^{f/f}$-1 mice, while circle symbols represent *CD19*$^{cre/+}$*Stat3*$^{f/f}$-2 mice. Statistical significance was evaluated by two-tailed unpaired *t* test. ***, $P < 0.001$; ****, $P < 0.0001$.

Absence of STAT3 leads to dysregulated B and T cell responses at 42 dpi

Due to observed immune perturbations in B cell-STAT3 KO mice at the early phase of chronic infection, we analyzed the B and T cell responses at a later 42 day timepoint. Mice produce virus-specific antibodies in response to MHV68 infection through a CD4+ T cell-dependent process (53, 54). The serum IgG levels were comparable between WT and B cell-STAT3 KO mice (Fig. 3A), but there was a significant decrease in virus-specific IgG in the serum of B cell-STAT3 KO mice (Fig. 3B). Accompanying this decrease, serum from B cell-STAT3 KO mice had a significantly reduced neutralization capacity by plaque reduction assay (Fig. 3C).

We previously reported that the latency defect in B cell-STAT3 KO mice was maintained even during the maintenance phase of infection at 42 dpi (42), and we confirmed this for *CD19*$^{cre/+}$*Stat3*$^{f/f}$-2 mice (Fig. S1). T cells and effector cytokines such as interferon (IFN)-γ control viral load during chronic infection with MHV68 (55). Activated, antigen-stimulated CD8+ T cells proliferate and differentiate into short-lived effector T cells or memory precursor effector T cells in response to infection. The B cell-STAT3 KO mice had an increase in short-lived effector T cells by both percentage and total numbers when compared to their WT littermates 42 dpi (Fig. 3D through E). We quantified the number of CD44^{hi}CD8+ T cells binding to MHC class I tetramers presenting the immunodominant epitope p79 derived from MHV68 ORF61 (Fig. 3F). The spleens of B cell-STAT3 KO mice had twice the number of p79-specific CD8+ T cells (Fig. 3G), and a greater proportion of these virus-specific T cells were short-lived effector T cells compared to WT mice (Fig. 3H). These unexpected aberrations in both the humoral and cell-mediated immune response confounded further mechanistic studies of B cell-STAT3 as a latency determinant and led us to develop an alternative mouse model to identify the B cell-intrinsic roles for STAT3.

Infection of a mixed bone marrow chimeric mouse model reveals B cell-intrinsic role for STAT3 in GHV latency establishment

Application of mixed BM chimeras to MHV68 infection has yielded important insight into the effects of B cell host determinants on infection (24, 26, 56). To better define the B cell-intrinsic role of STAT3, we generated mixed BM chimeras to analyze MHV68 latency in the context of the same adaptive immune response within each animal. To do this, CD45.2+ BM from *Stat3*$^{f/f}$*tdTomato*$^{stopf/f}$ mice (WT STAT3 B cells) and from *CD19*$^{cre/+}$*Stat3* $^{f/f}$*tdTomato*$^{stopf/f}$ mice (STAT3 KO B cells) was mixed 1:1 and transferred into CD45.1+ recipients that had been irradiated for myeloablation (Fig. 4A). The *tdTomato*$^{stopf/f}$ reporter results in tdTomato red fluorescent protein production after Cre recombinase expression. In the *CD19*$^{cre/+}$*Stat3* $^{f/f}$*tdTomato*$^{stopf/f}$ mice, tdTomato expression marks B cell with STAT3 deletion, allowing for discrimination of STAT3 WT B cells and KO B cells. Sorted tdTomato+ B cells were analyzed by immunoblot to confirm the loss of STAT3 protein specifically in the CD19+ tdTomato+ B cell population from *CD19*$^{cre/+}$*Stat3* $^{f/f}$*tdTomato*$^{stopf/f}$ mice but not *Stat3*$^{f/f}$*tdTomato*$^{stopf/f}$ WT B cells that lack Cre recombinase expression (Fig. S2A). TdTomato expression from CD19+ B cells (*Stat3*$^{f/f}$*tdTomato*$^{stopf/f}$) and CD19 haploinsufficiency (*CD19*$^{cre/+}$) did not impact MHV68 latency (Fig. S2B through D), and the *CD19*$^{cre/}$

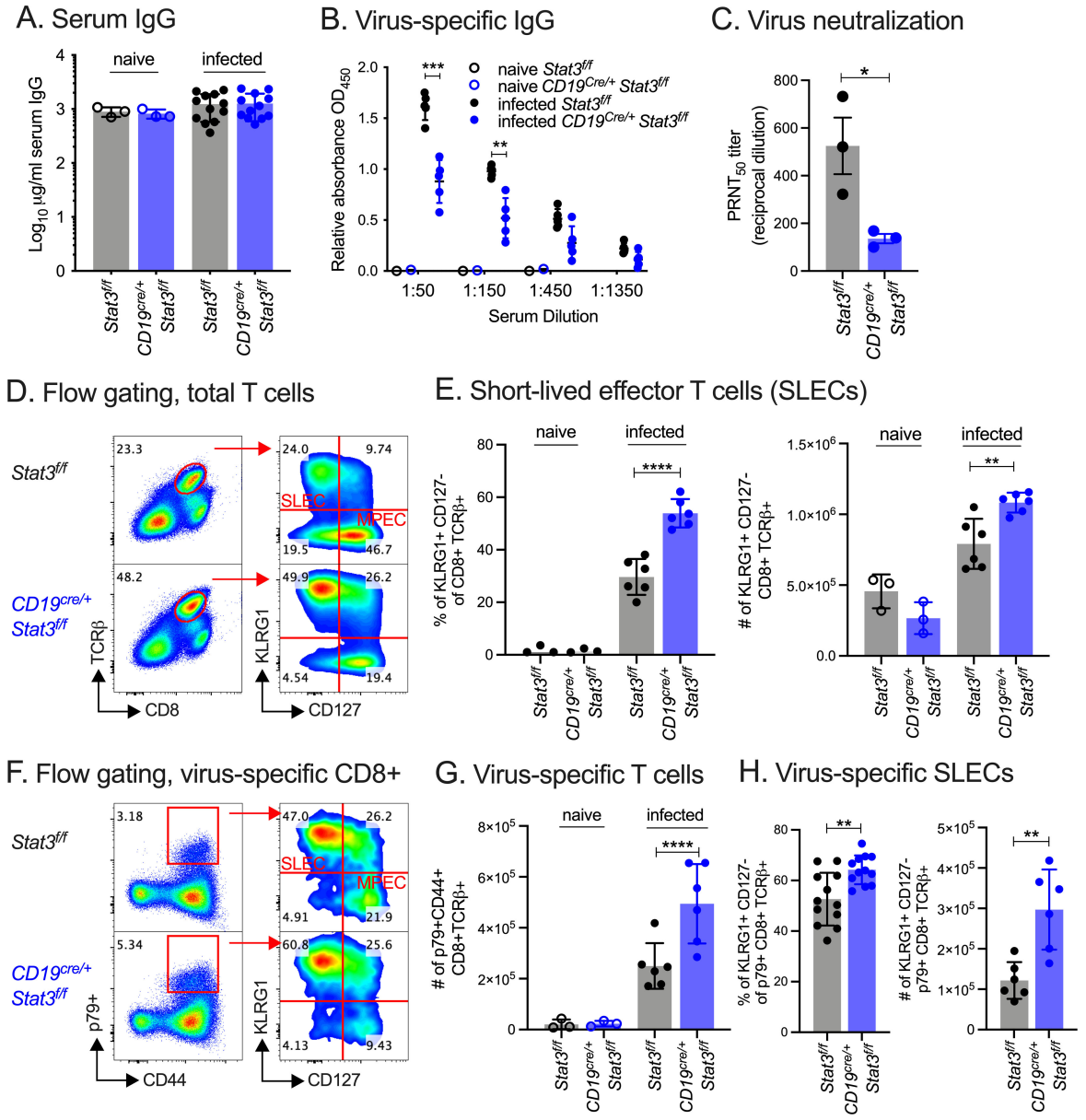

FIG 3 Reduced antibody response and heightened T cell response to MHV68 infection in B cell-STAT3 knockout mice. *Stat3*$^{f/f}$ (WT) and *CD19*$^{cre/+}$*Stat3*$^{f/f}$-2 (B cell-STAT3 KO) mice were infected with 1,000 PFU MHV68-H2bYFP by intraperitoneal inoculation and evaluated at 42 dpi. (A–B) Total serum IgG (A) or virus-specific IgG (B) from naive or MHV68-infected *Stat3*$^{f/f}$ and *CD19*$^{cre/+}$ *Stat3*$^{f/f}$ mice measured by ELISA. (C) Virus neutralization in serum as determined by a plaque reduction assay. The PRNT50 value is the dilution of serum to reach 50% neutralization of plaques. Symbols represent samples pooled from three independent experiments as biological replicates, each performed in technical triplicate. (D) Flow cytometry gating strategy for phenotyping short-lived effector CD8+ T cells (SLECs). (E) KLRG1+CD127− (SLEC) of CD8+ TCRβ+ T cells by percentage of splenocytes (left panel) and total numbers per spleen (right panel). (F) Flow cytometry gating strategy for p79 tetramer+CD44+ (virus-specific) SLECs. (G) Total p79 tetramer+ CD44+ (virus-specific) of CD8+ TCRβ+ per spleen. (H) Analysis of virus-specific SLECs by percentage of spleen (left panel) and total numbers per spleen (right panel). Data shown represent the mean ± SD (A, B, E, G, and H) of two to three independent experiments performed with four to seven mice per infected group and one to two mice for naive groups. For A, B, E, G, and H, each symbol represents an individual mouse. Statistical significance was evaluated by two-tailed unpaired *t* test (A–C, E, G, H). **, $P < 0.01$; ****, $P < 0.0001$.

$^{+}$*Stat3*$^{f/f}$*tdTomato*$^{stopf/f}$ reproduced the latency defect (Fig. S2E and F) observed for the *CD19*$^{cre/+}$*Stat3*$^{f/f}$ models (Fig. 1).

At 16 dpi, CD45.2+ splenocytes from the mixed BM chimeras were sorted to isolate tdTomato+ (STAT3 KO) and tdTomato− (STAT3 WT) B cells. Based on a limiting dilution, nested PCR for MHV68, KO B cells had a fivefold decrease in the frequency of

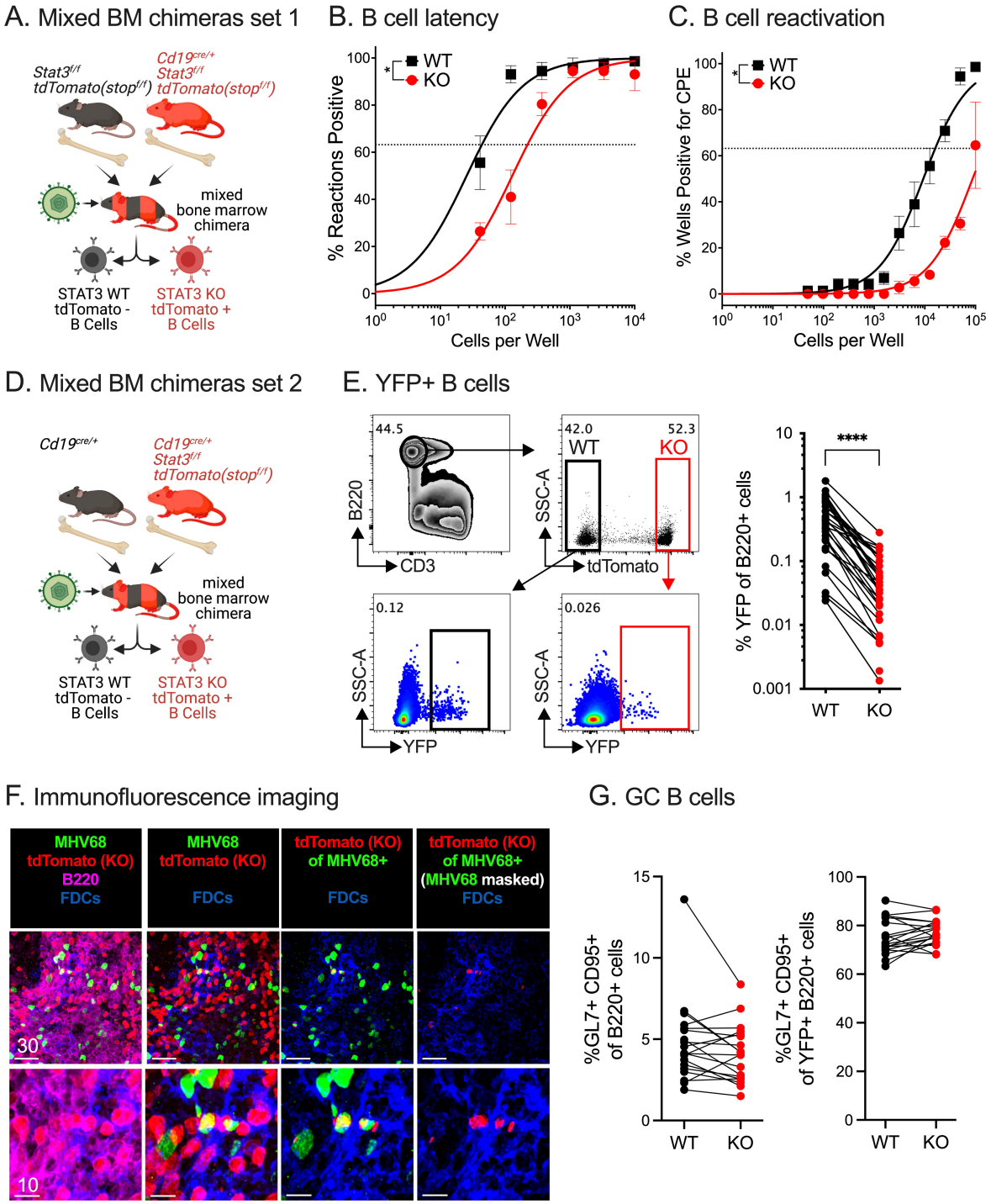

FIG 4 Mixed bone marrow chimera models reveal intrinsic requirement for STAT3 in B cells for efficient establishment of latency with MHV68. (A) Schematic depiction of the generation and infection of mixed BM chimera set 1 generated by reconstitution of CD45.1+ C57/BL6-recipient mice with bone marrow from CD45.2+ *Stat3*$^{f/f}$*tdTomato*$^{stopf/f}$ (WT) and *CD19*$^{cre/+}$*Stat3* $^{f/f}$*tdTomato*$^{stopf/f}$ mice (B cell-STAT3 KO). (B-C) Mixed BM chimeric set 1 mice were infected with 1,000 PFU MHV68-H2bYFP by intraperitoneal (i.p.) inoculation and evaluated at 16 dpi. (B) Single-cell suspensions of sorted tdTomato– (WT) and tdTomato+ (STAT3 KO) B cells were serially diluted, and the frequencies of cells harboring MHV68 genomes were determined using limiting dilution PCR. (C) Reactivation frequencies were determined by *ex vivo* plating of serially diluted sorted tdTomato– (WT) and tdTomato+ (STAT3 KO) B cells on an indicator monolayer. Cytopathic effect (CPE) was scored 3 weeks post-plating. For the limiting dilution analyses (B, C), curve fit lines were determined by non-linear regression analysis; frequency values were determined by Poisson analysis, indicated by the dashed line. Symbols represent the mean ± SEM of three independent experiments performed with six mice per infected group. (D) Schematic depiction of the generation and infection of mixed BM chimera set 2 mice generated by reconstitution of CD45.1+

(Continued on next page)

FIG 4 (Continued)

C57/BL6-recipient mice reconstituted with bone marrow from *CD19*$^{cre/+}$ and *CD19*$^{cre/+}$*Stat3*$^{f/f}$*tdTomato*$^{stopf/f}$ mice. (E–G) Mixed BM chimera set 2 mice were infected with 1,000 PFU MHV68-H2bYFP by i.p. inoculation and evaluated at 16 dpi. (E) Flow cytometry gating strategy for infected (YFP+) STAT3 WT (tdTomato–) and STAT3 KO (tdTomato+) B cells (B220+ CD3–) followed by quantitation of the frequency of infected B cells from mixed BM chimeras. (F) Confocal microscopy of frozen spleen sections of spleens from chimeric mice harvested on day 16 post-infection. For immunofluorescence imaging, tdTomato+ STAT3 KO B cells are red; MHV68-YFP+ cells are green; FDCs are blue; and B220+ B cells are magenta. Top panels, lower magnification images; bottom panels, higher magnification images of top panels. Far left panels, all colors; middle left omits B220 for easier visualization of tdTomato+ B cells; middle right panel, gated on the tdTomato cells infected with MHV68; far right panel is same as middle right panel but masks MHV68 signal (green) for easier visualization of tdTomato+ B cells. Scale bars = microns. (G) Quantitation of STAT3 WT and STAT3 KO germinal center B cells of total B cells (left panel) or of YFP+ B cells (right panel) by flow cytometry. Data for E and G represent the aggregated data from three independent experiments performed with six to seven mice per infected group. Each group of paired symbols represents the WT and KO B cell populations from one chimeric animal. Statistical significance was evaluated by paired *t* test. *, $P < 0.05$; ****, $P < 0.0001$.

genome-positive cells (average of 1/219) compared to their WT counterparts (average of 1/44) (Fig. 4B). The limiting dilution explant reactivation assay confirmed this decrease in latency establishment, but the frequency of spontaneous reactivation was not reduced further (Fig. 4C). These findings reinforce our initial findings (Fig. 1) and more rigorously demonstrate a B cell-intrinsic requirement for STAT3 in B cells for the efficient establishment of MHV68 latency.

To control for the haploinsufficiency of CD19 on the surface of *CD19*$^{cre/+}$ B cells, a second mixed BM chimera model was generated using donor *CD19*$^{cre/+}$*Stat3*$^{+/+}$ BM in combination with BM from *CD19*$^{cre/+}$*Stat3*$^{f/f}$*tdTomato*$^{stopf/f}$ mice (Fig. 4D). Flow cytometric analysis of the chimeras revealed an eightfold reduction in the frequency of MHV68-infected, YFP+ STAT3 KO B cells compared to their paired WT B cell counterparts (0.06% versus 0.51%) in the same animal at 16 dpi (Fig. 4E). Confocal microscopy of frozen tissue sections of infected spleen sections from mixed BM chimeras identified STAT3 WT (tdTomato–) and KO (tdTomato+, red) B220+ B cells interspersed throughout the tissue (Fig. 4F). The ratio of STAT3 WT:KO B cells was consistent with the mean 39:61 ratio of reconstitution for the respective WT:KO B cells determined by flow cytometry. TdTomato+ KO B cells were rarely detected in the YFP+ population, in contrast to frequent detection of YFP+ tdTomato- WT B cells. This is consistent with the failure of KO B cells to support latency in the splenic follicle based on limiting dilution PCR (Fig. 4B) and flow cytometric analysis of splenic single-cell suspensions (Fig. 4E). In contrast to the GC phenotype observed upon infection of mice that lacked STAT3 in all CD19+ cells (Fig. 2A), there was no difference in the frequency of GC B cells between the STAT3 WT and KO populations in the mixed BM chimera model (Fig. 4F and G; Fig. S2G and H). These findings substantiate STAT3 as a B cell-intrinsic latency determinant for GHV latency establishment in an *in vivo* model of infection wherein STAT3 WT and KO B cell populations reside in the same animal.

The STAT3-dependent transcriptional landscape of GC B cell genes

STAT3 directly regulates host genes conducive to proliferation and plasma cell differentiation in response to cytokines in the GC microenvironment, but the STAT3-dependent transcriptional landscape of GHV-infected GC B cells in the host has not been defined. Capitalizing on the ability to use flow cytometry to differentiate uninfected from YFP+ infected GC B cells, with and without STAT3 (tdTomato+), we sorted and collected specific subsets for RNA-sequencing. The CD45.2+ donor cells were gated on tdTomato to sort the STAT3 KO from WT B220+ B cells, followed by non-GC (GL7– CD95–) and GC (GL7+ CD95+) B cells (Fig. 5A). Last, the GC cells were sorted based on YFP to separate uninfected YFP– from infected YFP+ GC cells. In a principal component (PC) analysis, the non-GC and GC samples demonstrated the most difference along PC1, followed by separation of YFP– and YFP+ samples (Fig. 5B). The infected YFP+ WT GC segregated from the YFP+ STAT3 KO GC samples in PC2. Hierarchical clustering of the top 350 variable genes across all samples revealed binodal clustering of genes based on their regulation in non-GC versus GC B cells (Fig. 5C).

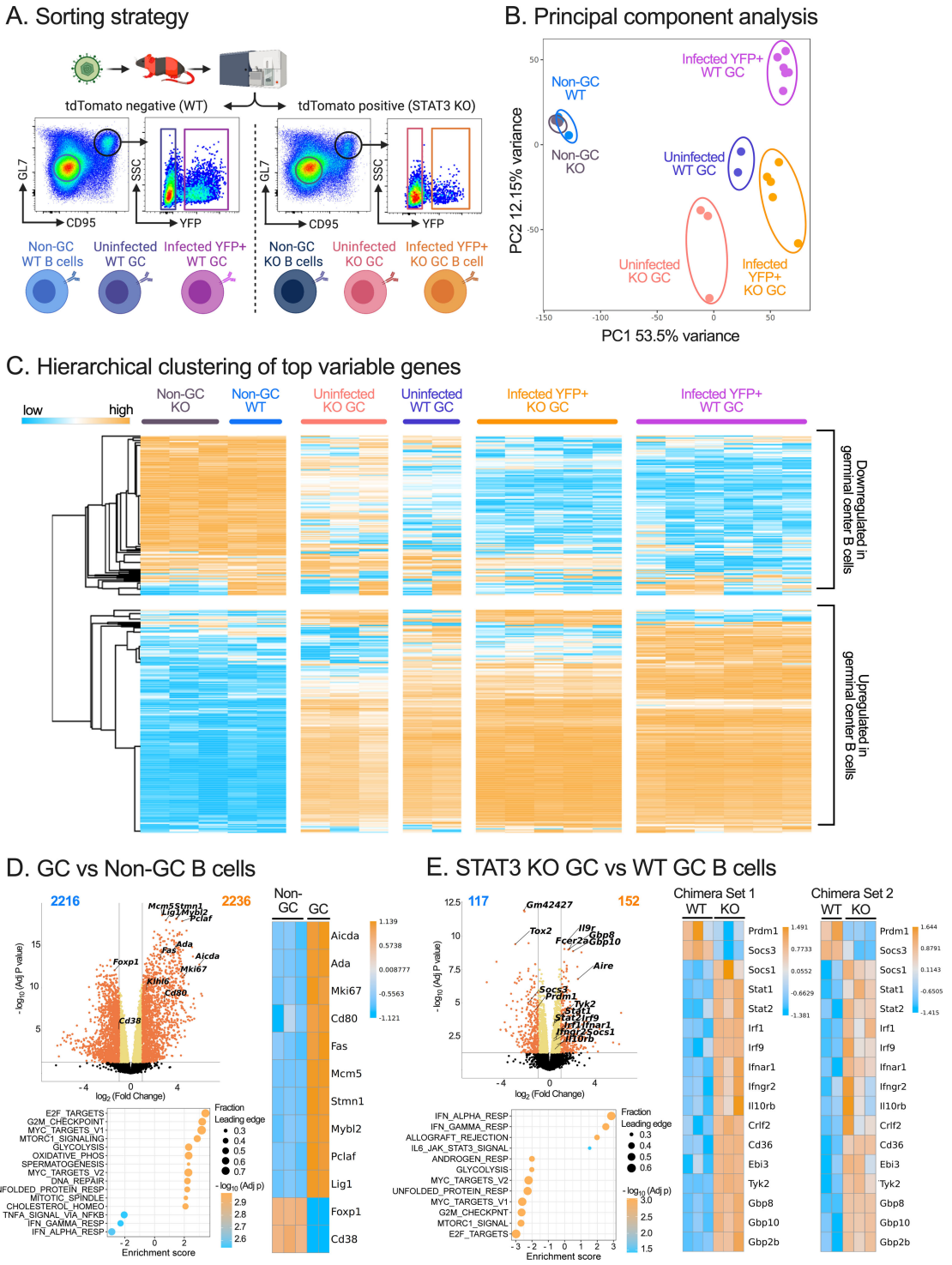

FIG 5 RNA-sequencing of B cells from infected mixed BM chimeric mice reveals transcriptional differences intrinsic to STAT3-ablated B cells. (A) Schematic depiction of flow cytometry sorting strategy for B cell populations from mixed BM chimeric mice. YFP+ infected and YFP− uninfected GL7+ CD95+ germinal center cells were sorted and collected from tdTomato− and tdTomato+ populations 16 dpi. Non-GC (GL7− CD95−) cells were also collected for tdTomato− and tdTomato+ populations. (B) Principal component analysis to analyze the clustering of RNAseq samples from the indicated flow sorted populations, mixed BM chimeric set 2. (C) Hierarchical clustering of the top 350 differentially expressed genes (DEGs) across all samples, mixed BM chimeric set 2. (D–E) For each, volcano plots with significance cutoffs displaying $\log_2$ fold change versus $-\log_{10}$ adj *P* value. Heatmaps display genes with adjusted *P* value ≤0.05 and at least twofold change between indicated comparisons. Gene set enrichment analysis (GSEA) panels display HALLMARK gene sets with adjusted *P* value ≤0.05, |NES| ≥2. Size of dot represents fraction of genes from the gene set that are leading edge genes in the specified comparison. (D) Bioinformatic analysis comparing GC

(Continued on next page)

FIG 5 (Continued)

and non-GC B cells, mixed BM chimeric set 2. Heatmap (right panel) of differentially regulated GC-specific genes curated from Broad Institute GSEA gene sets. (E) Bioinformatic analysis comparing uninfected STAT3 KO GC B cells to uninfected STAT3 WT GC B cells, mixed BM chimera set 2. Heatmaps (right panels) of DEGs in replicate RNAseq data sets from mixed BM chimera sets 1 and 2; genes listed detail hallmark IFNα response and STAT3-regulated genes.

A comparison of WT GC to WT non-GC B cells in a volcano plot that highlighted genes with a minimum twofold change and adjusted *P* value <0.05 identified the upregulation of GC-signature genes *Aicda, Mki67, Cd80,* and *Fas,* with downregulation of *Foxp1* and *Cd38* (57, 58). In a gene set enrichment analysis (GSEA), hallmark gene sets associated with proliferation, such as E2F targets, G2M checkpoint, MYC targets, and MTOR signaling, were positively enriched in the GC cells compared to the non-GC B cells, while interferon-α and IFNγ response pathways had a negative enrichment score (Fig. 5D).

Next, KO GC cells were compared to their WT GC counterparts. Genes encoding B cell surface proteins IL-9R (*Il9r*) and CD23 (*Fcer2a*) were highly upregulated upon loss of STAT3, while known STAT3 target genes *Socs3* and *Prdm1* were downregulated (Fig. 5E, upper left panel). Hallmark gene sets for G2M checkpoint, E2F targets, and MYC proliferative pathways were negatively enriched in the KO GC cells, in striking contrast to WT GC cells, and highlight the role of STAT3 as a driver of cell cycle and proliferation (Fig. 5E, lower left panel). Regarding upregulated gene sets, the IFNα and IFNγ response gene sets had the highest enrichment scores, indicating a heightened IFN profile in KO GC cells. An enhanced IFN response encompassed an increased transcript expression of IFNα and IFNγ receptors and downstream signaling molecules *Stat1, Stat2, Irf9,* and IFN-stimulated genes (ISGs) including *Ebi3, Irf1,* and *Gbp10* in both mixed BM chimera data sets (Fig. 5E, right panels). In summary, the loss of the master regulator STAT3 led to significant changes in the transcriptional landscape of GC cells, marked by the downregulation of genes driving proliferation and cell cycle progression and an upregulation of genes driving a type I and type II IFN response in the mixed BM chimera model.

The impact of MHV68 infection and STAT3 on GC B cell gene expression

Viral gene expression was tightly restricted in GC B cells, with very low levels of expression across the viral genome (Table S1). Although viral gene expression was minimal in GC cells at 16 dpi, there was a greater than fourfold higher expression level of genes with functions in immune modulation (*M3, mK3),* viral gene transactivation (*ORF57*), and viral DNA replication (*ORF6, ORF21, ORF59,* and *ORF61*) compared to the mean expression level of all viral ORFs (Fig. 6A; Fig. S3). Notably, ORF6 and ORF61 are the source of immunodominant CD8 T cell epitopes in infected C57BL/6 mice (59). However, there were no significant changes in the viral gene expression profile of infected GC B cells in the absence of STAT3.

MHV68 infection of WT GC cells led to a multitude of host transcriptional changes. Hierarchical clustering of DEGs comparing infected KO and WT GC cells revealed four distinct clusters of genes that demarcate the combined impact of infection and the status of STAT3 (Fig. 6B; Table S2). Genes in cluster I were upregulated by the presence of the virus in WT GC but to a lesser degree in infected STAT3 KO cells; genes of this cluster encode *Il10* and regulatory proteins, such as *Pik3cb* and *Ret*, in addition to mTOR pathway molecules *Asns, Cdkn1a, Cth,* and *Trib3* (Fig. 6B and C). Gene expression in clusters II and III was positively or negatively regulated by STAT3, respectively. Genes in cluster II include STAT3-regulated genes *Prdm1, S1pr1,* and *Socs3*, while genes in cluster III include the regulatory factor *Smad1* and the nucleotide biosynthetic molecule *Upp1* (Fig. 6B and C). Cluster IV genes such as *Fcer2a, Il9r, Aire, Vav3, Icos*, and numerous interferon response genes were downregulated by the virus in WT infection, but this virus-driven decrease was blocked in the absence of STAT3 (Fig. 6B and C).

We and others previously reported a bias in the B cell immunoglobulin (Ig) repertoire in the context of MHV68 infection; infected B cells exhibited immunoglobulin heavy chain V gene usage that was non-overlapping with uninfected cells and displayed bias

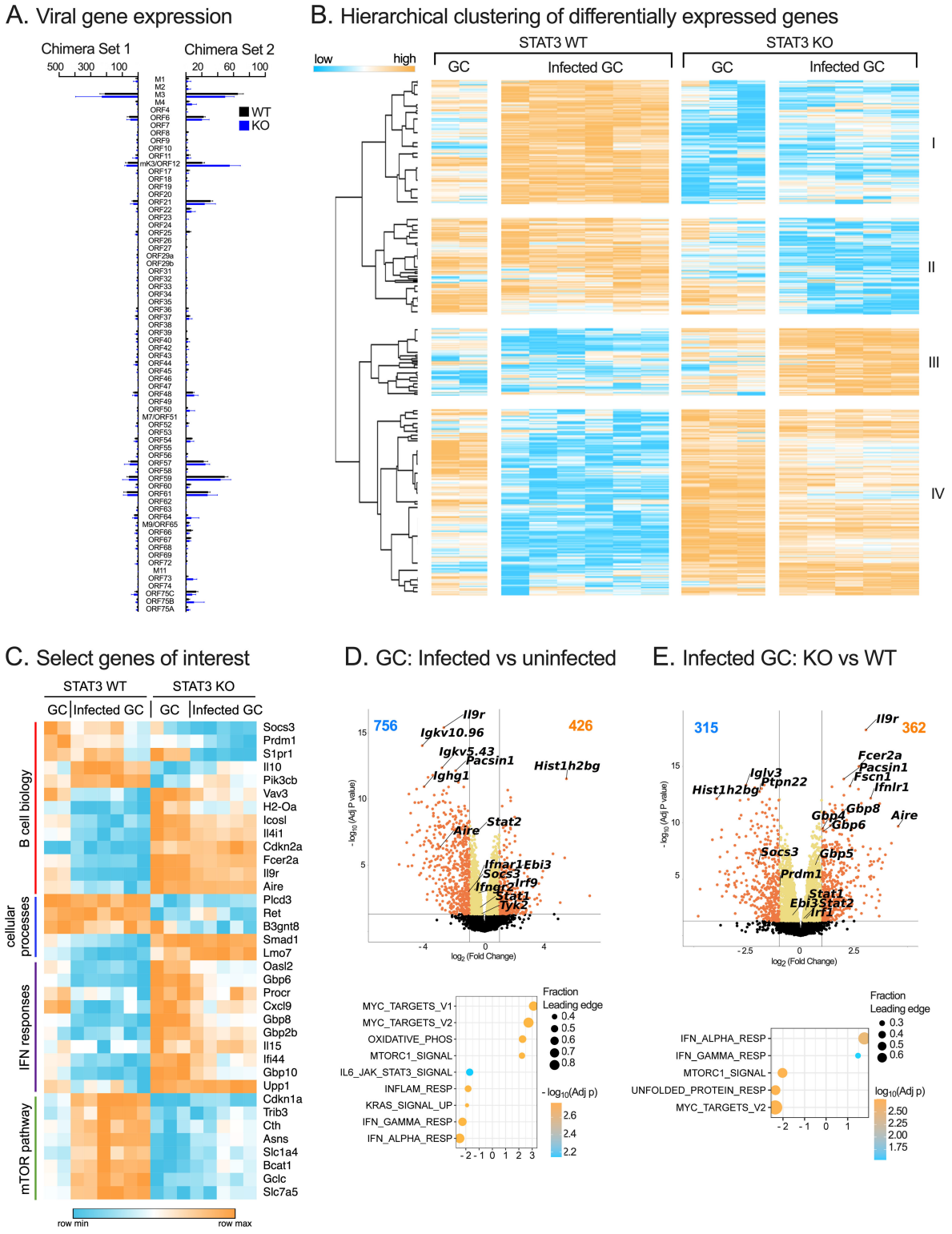

FIG 6 Loss of STAT3 leads to a heightened interferon response in germinal center B cells. (A) Viral gene expression of infected YFP+ cells sorted from WT and KO GC B cells from the two mixed BM chimera experiments. Bars represent the mean of the median-scaled CPM TMM values for each group of samples. (B) Hierarchical clustering of differentially expressed genes (DEGs) from the comparison of infected STAT3 WT and infected STAT3 KO GC B cells in mixed BM chimera set 2, with the addition of uninfected GC B cells and separated into four distinct clusters of gene expression patterns. Output generated in Morpheus, https://software.broadinstitute.org/morpheus. These were filtered to retain only genes with adj *P* value ≤0.05 and at least twofold change comparing infected WT and infected KO GC B cells. (C) Heatmap visualization of select gene expression across uninfected and infected GC samples in mixed BM chimera set 2. *Il10*

(Continued on next page)

FIG 6 (Continued)

and STAT3 target genes *Socs3* and *Prdm1* are included for reference. The remaining genes are DEGs from (B) or leading-edge genes common to both mixed BM chimera data sets. Leading edge genes from the hallmark IFNα response, IFNγ response, and mTOR signaling gene sets as revealed from pre-ranked GSEA of the infected KO GC versus infected WT GC B cell are noted, along with genes with roles in B cell biology and broader cellular processes. (D–E) Bioinformatic analysis comparing infected WT germinal center to uninfected WT GC B cells (D) and infected KO GC to infected WT GC B cells (E). Upper volcano plots display $\log_2$ fold change versus $-\log_{10}P$ value for mixed BM chimera set 2. *Hist1h2bg* reflects the H2b-YFP fusion gene delivered by the recombinant MHV68-H2bYFP reporter virus. Lower GSEA panels display hallmark gene sets with adj *P* value ≤0.05, |NES| ≥1.5 that were common to both mixed BM chimera data sets. Size of dot represents fraction of genes from the gene set that are leading edge genes in the specified comparison.

in lambda light chain (34, 60). Here, comparison of infected with uninfected WT GC cells revealed the downregulation of multiple Ig heavy chain and light chain V genes (Fig. 6D, upper panel). The predominant IgH V genes were distinct in the infected GC compared to their uninfected WT counterparts from both sets of BM chimera models (Fig. S4A and B). Additionally, we confirmed that infected cells utilize lambda light chain more frequently (Fig. S4C and D).

Broadly, the comparison of infected to uninfected WT GC B cells by volcano plot revealed more host genes were downregulated (756 genes) than upregulated (426 genes) (Fig. 6D, upper panel). Loss of STAT3 in B cells altered the infected GC profile, leading to upregulation of 362 genes and downregulation of 315 genes ((Fig. 6E, upper panel). GSEA identified positive enrichment for MYC targets, oxidative phosphorylation, and MTOR signaling upon MHV68 infection of WT GC B cells, highlighting the increased expression of genes involved in cell cycle progression and metabolism (Fig. 6D, lower panel), similar to reports for primary B cells newly infected with EBV (61). In contrast, MYC and MTOR gene sets were negatively enriched when comparing infected KO and infected WT GC cells, suggesting that signatures of proliferation in the infected B cells are dependent on STAT3 (Fig. 6E, lower panel). Consistent with the known impacts of MHV68 in blocking host IFN responses (62–67), there was a negative enrichment for genes involved in response to IFNα and IFNγ in the infected WT GC B cells (Fig. 6D). This includes the downregulation of signaling molecules *Stat2* and downstream ISGs *Gbps 2b, 6, 8,* and *10, Oasl2, Tap1, Usp18,* and *Trim21* (Fig. 6C; Fig. S5). STAT3 negatively regulates the type I IFN response by induction of the suppressor of cytokine signaling factor 3, *Socs3*, that suppresses STAT1 and STAT2, in addition to repression of *Irf9* transcription and by direct binding of STAT1 partners (68–70). *Socs3* was downregulated in the absence of STAT3 in sorted GC B cells (Fig. 6C and E), as validated by qRT-PCR in B cells from infected mice (Fig. S6). Consistent with decreased expression of *Socs3*, GSEA revealed an enrichment in genes associated with IFNα and IFNγ responses in infected KO compared to infected WT GC cells in mixed BM chimera samples (Fig. 6E; Fig. S5). Taken together, MHV68 infection reprograms GC B cells *in vivo* to upregulate networks that promote proliferation while impairing genes associated with IFN responses. This virus-induced signature is reversed in the absence of STAT3.

Reduction of CD23 expression on infected B cells is influenced by STAT3

A comparison of infected KO GC with infected WT GC cells uncovered significant changes in genes with functional links to biological processes of B cells in the absence of STAT3, including regulatory proteins (*Socs3*, *Pik3b*, *Vav3*, and *Cdkn2a*), transcription factors (*Prdm1* and *Aire*), and cell surface proteins that mediate responses to the microenvironment to influence B cell differentiation (*S1pr1*, *Il9r*, and *Fcer2a*). (Fig. 6C and E, upper panel). *Fcer2a* encodes the low-affinity IgE receptor commonly known as CD23, a surface marker that has been reported to promote B cell activation and to function as a negative regulator of IgE responses (71–73). In agreement with RNAseq, *Fcer2a* transcript levels were markedly upregulated in KO B cells compared to WT B cells that were isolated from naive and MHV68-infected mice (Fig. S6C and D). Further validation was revealed by flow cytometric analysis of CD19+ B cell subsets. The frequency of $CD23^{hi}$ B cells was significantly reduced in WT-infected mice but only slightly diminished in B cell-STAT3 KO mice (Fig. 7A, right panel). The WT B cells directly infected with MHV68 (YFP+) had

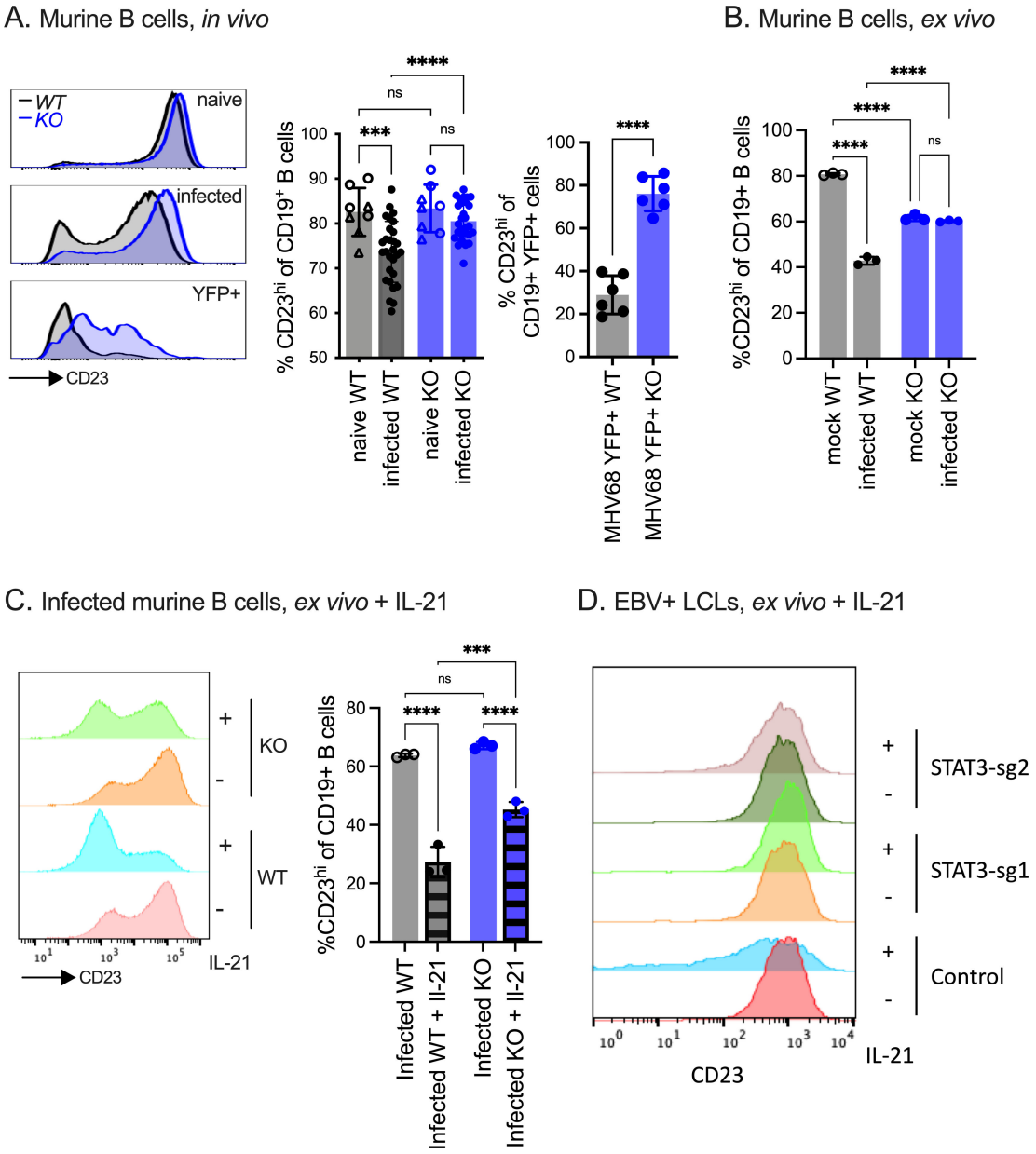

FIG 7 IL-21-stimulated reduction of CD23 surface expression is dependent on STAT3. (A) Left panel, histogram depiction of surface CD23 expression on B cells from naïve mice compared to B cells or YFP+ B cells from infected WT (*Stat3*$^{f/f}$) or B cell STAT3 KO (*CD19*$^{cre/+}$*Stat3*$^{f/f}$) mice at 16 dpi based on flow cytometric analysis. Middle and right panels are the quantitation of the frequency of CD23^{hi} B cells from the indicated populations. Symbols represent individual mice ± SD from one (YFP+ B cells) to six (B cells from naïve and infected mice) independent experiments performed with three to seven mice per infected group and one to two mice per naive groups. (B) Frequency of *Stat3*$^{f/f}$ and *CD19*$^{cre/+}$*Stat3*$^{f/f}$ B cells with CD23^{hi} expression upon mock or MHV68 infection, 3 dpi. (C) Left panel, histogram depiction of CD23^{hi} B cells from anti-CD40 MHV68-infected cultures treated concurrently without or with IL-21 for 3 days, as indicated. Right panel, gated histogram data summarized in bar graphs. (D) Histogram depiction of CD23 surface expression on EBV+ GM12878 lymphoblastoid B cell lines (LCLs) that express Cas9 in addition to control sgRNA or sgRNA targeting STAT3. Cells were mock stimulated or stimulated with IL-21 (100 ng/mL) for 6 days. Statistical significance was evaluated by one-way ANOVA followed by Sidak's multiple comparisons or an unpaired one-tailed *t* test for the YFP+ cell analysis; ***, $P < 0.001$; ****, $P < 0.0001$; ns, $P > 0.05$.

a threefold lower CD23^{hi} expression compared to STAT3 KO cells (Fig. 7A). Next, we examined whether MHV68 infection of primary B cells *ex vivo* impacts CD23 surface expression via STAT3. Primary B cells from WT and B cell-STAT3 KO mice were infected and analyzed at 3 dpi. MHV68 infection led to an increase in STAT3-Y705 phosphorylation in the YFP+ subset, indicating that direct infection activates STAT3 (Fig. S7A). Infection

also led to a twofold decrease in the frequency of WT B cells with CD23^{hi} expression (Fig. 7B) and a fourfold decrease in *Fcer2a* transcript levels (Fig. S6E), but no significant change was observed between uninfected and infected B cells lacking STAT3. Taken together, the repression of CD23 transcript and surface expression on murine B cells upon MHV68 infection are mediated in part by STAT3.

IL-21 signaling in B cells is necessary for the efficient establishment of latency with MHV68 (24). IL-21 is a well-known activator of STAT3 (Fig. S7B) that promotes B cell activation and germinal center processes leading to plasma cell differentiation (74–76). Consistent with previous reports (71, 77), activation of CD40 signaling led to the upregulation of CD23 from 37% to 94% of WT (*Stat3*$^{f/f}$) B cells, while IL-21 in combination with α-CD40 significantly reduced CD23^{hi} expression to 60% on WT B cells (Fig. S7C). This IL-21-stimulated downregulation was largely reversed in STAT3 KO B cells (*CD19*$^{cre/+}$ *Stat3*$^{f/f}$). In the context of MHV68 infection, IL-21 in combination with α-CD40 led to a twofold reduction in CD23^{hi} WT B cells that was partially restored in the absence of STAT3 (Fig. 7C). The analysis of this STAT3-dependent IL-21 downregulation of CD23 was extended to an EBV+ lymphoblastoid B cell line (LCL), which highly expresses CD23 (78). Surface CD23 levels were greatly diminished on LCL GM12878 upon a 6-day treatment with IL-21. However, CRISPR-mediated knockout of STAT3 rendered two independent LCL cultures non-responsive to IL-21-induced loss of surface CD23 (Fig. 7D). These findings reveal a role for STAT3 in regulating the CD23 surface molecule on B cells in response to IL-21 in the context of GHV infection.

DISCUSSION

Here, we aimed to identify transcriptional and functional roles for STAT3 in B cells newly infected with a gammaherpesvirus *in vivo*. First, we verified a significant defect in latency establishment in two strains of B cell-STAT3 knockout mice. This decrease in virus latency was accompanied by an increase in GC B cells and a reduction of infected plasma cells. Our analyses identified altered GC architecture in B cell-STAT3 KO mice, along with reduced virus-specific antibody production, and a heightened CD8 T cell response. This perturbed immune response led us to develop a mixed BM chimera model wherein STAT3 KO B cells and WT B cells were both present as potential reservoirs of latency in the same host microenvironment. B cells lacking STAT3 were not able to compete with their wild-type counterparts to support GHV latency at 16 dpi. To dissect the transcriptional consequences of STAT3 loss, RNA sequencing was performed on sorted STAT3 WT and KO GC B cells, with and without MHV68 infection. Our analysis revealed that STAT3 targets pathways associated with proliferation and interferon responses in GC B cells infected with MHV68.

We previously reported a requirement of STAT3 to support the efficient establishment of latency in a B cell-STAT3 KO mice model (42). Briefly, infection of B cell-STAT3 KO mice led to a reduction in splenic latency and an increase in GC B cells 16 dpi. Here, we expand upon these results in a second strain of STAT3 KO mice and report new findings of alterations in the virus-specific immune response that call attention to the role for STAT3 in GC development after virus infection. Immunization of STAT3-KO mice with ovalbumin led to a notable decrease in GC B cells, short-lived GC structures, and a decrease in plasma cells (79). MHV68 infection resulted in an increase in total GC B cells in B cell-STAT3 KO mice, but immunofluorescence of infected spleen sections revealed smaller follicles with less organized GCs in B cell-STAT3 KO mice (Fig. 2D). MHV68 infection of mice leads to an increase in highly proliferative centroblasts compared to centrocytes within the infected GC population, as well as the total GC population (22, 24). In the absence of STAT3, we observed a reduced frequency of centroblasts in naive mice, as well as those infected with MHV68, with the ratio further skewed toward centrocytes in the infected GC population (Fig. 2C). The aberrant GC architecture and the reduction in centroblasts at 16 dpi along with the reduction in virus-specific antibodies suggest that GC cycling between dark and light zones may be disrupted in GCs of mice lacking STAT3 in B cells. Recently, STAT3$^{fl/fl}$CD23^{Cre} mice were reported to have defects

in GC organization due to aberrant light zone to dark zone recycling upon antigen immunization or influenza virus infection (80). In an analysis of the STAT3-regulated GC transcriptome, pathways involving Myc, E2F, and mTORC1 signaling were strongly enriched (80), demonstrating common biologic roles for B cell STAT3 identified from our analysis of MHV68-infected *CD19*$^{cre/+}$*Stat3*$^{f/f}$ mouse models.

In the GC reaction, B cells differentiate and exit the GC as class-switched, long-lived memory B cells or antibody-secreting plasma cells. STAT3 coordinates the upregulation of *Prdm1*, encoding Blimp-1, which is a master regulator of B cell differentiation to plasma cells in response to IL-21 (50, 51). These plasma cells are a source of MHV68 reactivation in the spleen (52), and long-lived plasma cells are a long-term latency reservoir in the bone marrow, which led us to examine plasma cells in the B cell-STAT3 KO mice. There was no difference in plasma cell frequency at 16 dpi, although there was a decrease in infected (YFP+) plasma cells in B cell-STAT3 KO mice. This phenotype was also reported for MHV68 infection of IL-21R KO mice, where IL-21 signaling is necessary for latency establishment (24). Regarding chronic infection at 42 dpi, there was a significant reduction in virus-specific IgG (Fig. 3B) and virus-neutralizing activity in serum (Fig. 3C) from B cell-STAT3 KO mice. We note that the defect in B cell infection was observed even earlier at 12 dpi, but the limited number of infected cells precluded an in-depth analysis of this population.

The latency-associated M2 protein of MHV68 is critical for viral latency establishment in mice (81, 82). M2 induces high levels of IL-10 secretion in B cells and drives B cells to differentiate into plasmablasts *in vivo* (38–40). IL-10 is an anti-inflammatory cytokine that suppresses natural killer and T cell effector responses (83). An increase in virus-specific, short-lived effector CD8+ T cells (SLECs) was noted in the B cell-STAT3 KO mice at 42 dpi (Fig. 3H). The heightened virus-specific CD8+ T cell response may be a byproduct of the latency defect in B cell-STAT3 KO mice, driven by a reduction in MHV68 M2-driven production of the immunosuppressive cytokine IL-10. This finding is consistent with reports of increased virus-specific effector T cells in mice infected with a recombinant MHV68 virus that does not express the viral M2 protein (38).

Mixed BM chimeras have been employed to bypass immune defects caused by global deletion of signaling molecules CD40 and IL-21R or NF-κB p50 (24, 26, 56). Here, BM from STAT3 B cell-competent and -ablated mice was mixed to create an *in vivo* model wherein STAT3 WT and KO B cells are simultaneously evaluated for their ability to support latency, in the context of the same microenvironment and immune response to infection. This model reveals that the loss of STAT3 leads to a marked reduction in MHV68+ B cells (Fig. 4B and E), confirming that STAT3 is required to promote B cell latency by GHV in the GC. This rigorous analysis supports STAT3 as a B cell-intrinsic host factor essential for latency establishment in primary B cells.

This is the first report of an unbiased transcriptional profile of MHV68-infected GC B cells. We capitalized on our ability to distinguish STAT3 KO B cells from WT counterparts based on Cre-inducible tdTomato expression in STAT3 KO B cells and the YFP reporter gene from MHV68-H2bYFP. Fluorescence-activated cell sorter (FACS) sorting for non-GC and GC subsets, with and without STAT3, with and without infection, followed by RNAseq enabled us to define the multitude of changes to the transcriptional landscape of GC B cells driven by the virus and those changes that are dependent on STAT3 (Fig. 5C). GSEA of GC B cells revealed a virus-driven enrichment for MYC targets and metabolic processes of oxidative phosphorylation and mTOR, while IFNα and γ responses are diminished. MYC plays a major role in GC processes, regulating GC B cell entry and cycling between dark and light zones (84). Absence of MYC leads to reduced numbers of affinity-matured B cells within the GC. The impairment of MYC leads to the collapse of established GCs (85). Comparing STAT3 KO and WT GC B cells, there was a negative enrichment for MYC target genes by GSEA, consistent with the role for STAT3 in MYC-driven proliferation (86, 87).

MHV68 encodes numerous proteins to bypass the IFN response and promote replication and latency. MHV68 ORF11 and ORF36 interfere with IRF3 binding, blocking the transcription of IFNβ (63, 66). In addition, MHV68 ORF54 induces degradation of

IFNAR1 to block IFN signaling (64), while the latency protein M2 impairs downstream IFN signaling by inducing the downregulation of STAT1 and STAT2 (62). We observed low transcript levels of these ORFs in YFP+ GC cells at 16 dpi (Fig. 6A). A consistent finding in the comparison of STAT3 WT and KO GC B cells was the positive enrichment for IFN response pathways in uninfected and infected STAT3 KO B cells. IFN responses restrict MHV68 latency through the induction of interferon-stimulated genes, which typically promote an antiviral state (5, 88–91). Host factors that restrict MHV68 infection include those that promote IFN production like IRF3 and IRF7, and those that respond to IFN to directly induce ISG transcription like IRF1, STAT1, and STAT2 (62, 65, 92–95). Mice lacking STAT1, IFN-αβ receptor, or combination IFN-αβ and IFN-γ receptors succumb to infection with MHV68 (96), stressing the importance of the IFN response in combating the virus. In the absence of STAT3, there was an upregulation of ISGs such as *Oasl2* and the family of guanylate-binding proteins (GBPs). Many of these ISGs have known antiviral function; the human homolog of murine *Gbp2b* is human GBP1, and it was recently reported to block KSHV capsid transport by disrupting cytoskeletal actin networks (97). However, ISGs such as *Usp18* and *Trim21* that negatively regulate the IFN response were also upregulated (98, 99). A subset of patients with autosomal dominant hyper-IgE syndrome caused by loss-of-function mutations in STAT3 have been observed to develop a lupus-like syndrome involving heightened type I IFN responses (100). Further studies are required to clarify the net impact of these dysregulated ISGs on early events in gammaherpesvirus infection in *de novo*-infected primary B cells. STAT3 has been reported to negatively regulate the type I and II IFN responses by upregulating *Socs3*, repressing the transcription of *IRF9, STATs 1,* and *2*, and competing for binding with STAT1 to reduce ISGF3 transcriptional complex formation (68–70). While we observed consistent downregulation of *Socs3* in the absence of STAT3 in GC B cells of infected mice, the mechanism by which STAT3 suppresses IFN responses in MHV68-infected B cells, via either direct or indirect regulation, requires additional investigation.

The loss of STAT3 in GC B cells led to the downregulation of known STAT3 target genes, *Prdm1*, *S1pr1,* and *Socs3*, but also revealed the dysregulation of *Il9r* that encodes the receptor for IL-9 and *Fcer2a* that encodes CD23, the low-affinity IgE receptor. We observed that IL-21 suppresses CD23 expression in primary B cells at least in part through STAT3, consistent with transcript upregulation previously reported in an RNAseq data set of a diffuse large B cell lymphoma cell line treated with an shRNA targeting STAT3 (68). CD23 was downregulated in total splenic B cells upon MHV68 infection in mice and upon *ex vivo* infection of primary B cell cultures, even more so in the directly infected cells (Fig. 7A). CD40-ligation leads to the induction of CD23 on the surface of activated B cells (71). We observed that IL-21 reversed CD40 induction of CD23 in a STAT3-regulated manner, leading us to postulate that STAT3 is repressing CD23 expression through IL-21 signaling. Hyper-IgE syndrome patients have autosomal dominant loss-of-function mutations in STAT3, in whom naive and memory B cells are noted to have heightened CD23 surface levels (101). Future studies are needed to define the STAT3-dependent mechanism of CD23 downregulation in response to infection or IL-21. While the functional consequence of CD23 loss for B cells infected with MHV68 is unclear, caution is warranted when using CD23 to demarcate follicular B cells in the context of MHV68 infection.

EBNA2, a key latency-associated transactivator and transforming factor of EBV, and RTA, the master lytic transactivator of KSHV, each upregulate the *CD23* promoter through interactions with host RBP-Jkappa (102–104). CD23 expression is an indicator of B cell activation and surface CD23 complexes with surface CD21 and IgE (71, 73). Soluble CD23 (sCD23) is released upon metalloproteinase cleavage and mediates activation and differentiation of lymphocytes (72). sCD23 regulates IgE synthesis in human B cells, likely by binding CD21 and membrane IgE (105). Membrane and sCD23 are induced by RTA and EBNA2 (102, 106), and transfer of conditioned media containing sCD23 leads to activation of lymphocyte cultures (102). EBV+ LCLs express LMP1, a potent activator of STAT3, and EBNA2, a known activator of STAT3 and inducer of CD23 (107, 108). IL-21

treatment promotes the proliferation of EBV+ diffuse large B cell lymphomas, inducing LMP1, STAT3 activation, and *MYC* expression (109). Our finding that IL-21 treatment led to CD23 downregulation in EBV+ LCLs that retain STAT3 but not in those silenced for STAT3 expression suggests that CD23 induction by EBNA2 is lost in the absence of IL-21-induced STAT3 activation. Taken together, these findings suggest that a dynamic shift in STAT3 signaling occurs upon engagement of GHV-infected B cells with the GC cytokine IL-21. One outcome is the reduction in the levels of CD23, a B cell activation factor that has two mechanisms of action. Determining the consequences of these changes, and whether CD23 functions directly via receptor-mediated signaling on the infected B cell or indirectly via sCD23 shed into the GC microenvironment, will require careful delineation.

Our study highlights STAT3 signaling as a critical host pathway commandeered by GHVs to promote latency. We report that the requirement for STAT3 in MHV68 latency establishment is intrinsic to the infected B cell. STAT3 is activated upon MHV68 infection, and those infected B cells have gene signatures that partially overlap with signatures of virus-driven reprogramming reported for EBV and KSHV (110, 111). Understanding the virus-host interplay during long-term latency and how the GHVs utilize host factors and pathways to develop cancers is paramount. KSHV miRNAs block STAT3, and inhibition of STAT3 increases reactivation from latency (112). While there is a long-term latency defect in B cell-STAT3 KO mice 42 dpi, the role of STAT3 in the maintenance of MHV68 has not been investigated. A recent study reveals a role for the STAT3-activating cytokine IL-16 in inhibiting MHV68 reactivation through the STAT3-p21 axis (113). Though the use of JAK and direct STAT3 inhibitors show promise in clinical trials, deeper understanding of the role of STAT3 in viral persistence is required, as some GHV cancers may lose their dependency on STAT3 (114). This study provides a comprehensive examination into understanding signaling downstream of STAT3 in GHV infection *in vivo* by transcriptional profiling of the major B cell latency reservoir. Future studies to delineate factors downstream of STAT3 in the context of GHV latency will reveal new avenues of treatment important for the prevention and treatment of GHV-driven malignancies.

MATERIALS AND METHODS

Animal models

Strain 1 designates *Stat3*$^{f/f}$ mice with exons 12–14 flanked by *loxP* elements (44), and Strain 2 designates *Stat3*$^{f/f}$ mice with exons 18–20 flanked by *loxP* elements [B6.129S1-*Stat3*^{tm1Xyfu}/J] (The Jackson Laboratory, Bar Harbor, ME) (45). *CD19*$^{cre/cre}$ mice [B6.129P2(C)-Cd19 $^{tm1(cre)Cgn}$/J] (Jackson) were crossed with Strain 1 and Strain 2 mice to generate *Stat3*$^{f/f}$*CD19*$^{cre/+}$-1 and -2 mice, respectively. *Stat3*$^{f/f}$ and *Stat3*$^{f/f}$*CD19*$^{cre/+}$ mice used in pathogenesis experiments were littermates derived from crossing *Stat3*$^{f/f}$ mice with *Stat3*$^{f/f}$ mice heterozygous for *CD19*^{cre}; sexes were randomly assigned to experimental groups.

TdTomato$^{stopf/f}$ mice [B6.Cg-*Gt(ROSA)26Sor*$^{tm14(CAG-tdTomato)Hze}$/J] (Jackson) were crossed with *Stat3*$^{f/f}$ *CD19*$^{cre/+}$ mice for multiple generations to generate *CD19*$^{cre/+}$*Stat3* $^{f/f}$*tdTomato*$^{stopf/f}$ mice. First, a male *CD19*$^{cre/+}$*Stat3*$^{f/f}$ mouse was crossed with a female *tdTomato*$^{stopf/f}$ mouse generating progeny mice that were heterozygous at the *CD19*, *Stat3,* and *tdTomato* loci. Next, an F1 cross was set up with a male and female mouse of the following genotypes: *CD19*$^{cre/+}$*Stat3* $^{f/+}$*tdTomato*$^{stopf/+}$ and *CD19*$^{+/+}$*Stat3* $^{f/+}$*tdTomato*$^{stopf/+}$. Progeny mice from this pairing were then set up for an F2 cross, consisting of a male and female pairing of the following genotypes: *CD19*$^{cre/+}$*Stat3* $^{f/+}$*tdTomato*$^{stopf/f}$ and *CD19*$^{+/+}$*Stat3* $^{f/+}$*tdTomato*$^{stopf/f}$. Mice produced from this F2 cross maintained floxed alleles for both the *Stat3* and *tdTomato* loci as follows: *CD19*$^{cre/+}$*Stat3* $^{f/f}$*tdTomato*$^{stopf/f}$ and *CD19*$^{+/+}$*Stat3* $^{f/f}$*tdTomato*$^{stopf/f}$. To maintain the colony and produce mice for experiments, parings were set up which consisted of the following genotypes: *CD19*$^{cre/+}$*Stat3* $^{f/f}$*tdTomato*$^{stopf/f}$ and *CD19*$^{+/+}$*Stat3* $^{f/f}$*tdTomato*$^{stopf/f}$. Mice were backcrossed for at least five generations before experiments were performed.

CD19$^{cre/+}$ mice were generated by crossing *CD19*$^{cre/cre}$ mice with C57BL/6 mice. Ly5.1 (CD45.1) [B6.SJL-Ptprca Pepcb/BoyJ] (Jackson) were the recipient mice for bone marrow chimera studies. All mice were bred at the Stony Brook University Division of Laboratory Animal Research facility or the National Institutes of Health Division of Veterinary Resources, unless stated otherwise. Mice were housed in a specific pathogen-free environment, and all mouse experiments were performed in accordance with guidelines under protocols approved by the Institutional Animal Care and Use Committee of Stony Brook University and the NCI Animal Care and Use Committee.

Generation of mixed bone marrow chimeric mice

Recipient Ly5.1 (CD45.1) [B6.SJL-Ptprca Pepcb/BoyJ] (Jackson) at 6 weeks of age were gamma irradiated with 900 rads, in split dose. Next, mice were injected retro-orbitally with two million bone marrow cells isolated from donor *CD19*$^{cre/+}$*Stat3* $^{f/f}$*tdTomato*$^{stopf/f}$ (KO) and *Stat3*$^{f/f}$*tdTomato*$^{stopf/f}$ (WT) mice at a 50% WT:50% KO bone marrow ratio for the first set of chimeras or with five million bone marrow cells isolated from donor *CD19*$^{cre/+}$*Stat3* $^{f/f}$*tdTomato*$^{stopf/f}$ (KO) and *CD19*$^{cre/+}$ (WT) mice at a 30% WT:70% KO bone marrow ratio for the second set of chimeras. All female mice were used; there is no discernible difference between male and female mice with respect to establishment of MHV68 latent infection. Mice were treated with acidified water 2 weeks prior to and after irradiation. Verification of chimerism was performed 6 weeks post transfer through collection of blood by submandibular bleed, followed by flow cytometry. The mean reconstitution ratio was 66% WT:34% KO cells for the first set of chimeras and 39% WT:61% KO for the second set of chimeras.

Cells and viruses

Recombinant MHV68 expressing H2bYFP fusion protein (rMHV68-H2bYFP) was used for the infection (115). Mice (8–12 weeks old) were infected by intraperitoneal injection with 1,000 PFU in 0.5 mL under isoflurane anesthesia. Mouse spleens were homogenized, treated to remove red blood cells, and passed through a 100-µm-pore-size nylon filter. For *ex vivo* experiments, flow sorting, and RNA-sequencing, splenocytes were subject to negative selection to enrich for B cells (Pan B Cell Isolation Kit; Stemcell, Vancouver, BC, Canada). Cells were counted using Vi-CELL BLU Cell Viability Analyzer (Beckman Coulter, Pasadena, CA). Blood was collected posthumously by cardiac puncture. Serum was collected after a centrifugation at 20,000 × *g* for 20 min at room temperature.

For STAT3 knockout in the EBV+ LCLs, single-guide RNA (sgRNA)-directed CRISPR-Cas9 gene knockout was performed as previously described (116). In brief, two independent STAT3 targeting sgRNAs (GAGACCGAGGTGTATCACCA and AACATGGAAGAATCCAACAA) from Brunello library (117) were cloned into pLentiGuide-puro (a gift from Feng Zhang, Addgene # 52963). Lentiviruses were produced by transfection of 293T cells and used to transduce Cas9+ GM12878 LCLs as previously described (116, 118). In parallel, GM12878 were transduced with control lentivirus expressing an sgRNA targeting GFP (pXPR-011, a gift from John Doench). Transduced LCLs were selected by puromycin (3 ug/mL, Invitrogen) for 3 days.

Cell stimulation and *ex vivo* virus infection

For cytokine stimulations *ex vivo,* primary murine splenocytes were harvested from spleens of *Stat3*$^{f/f}$ and *Stat3*$^{f/f}$*CD19*^{cre} mice. Single-cell suspensions were subjected to negative selection to enrich for B cells (Pan B Cell Isolation Kit; Stemcell, Vancouver, BC, Canada). Primary B cells were plated in a 96-well plate at a concentration of 4–5 × 10^5 cells/mL, in 200 µL of primary B cell media (RPMI 1640 supplemented with 20% FBS, HEPES, non-essential amino acids, sodium pyruvate, penicillin/streptomycin, L-glutamine, β-mercaptoethanol). rMHV68-H2bYFP was added at an MOI of 20 in the presence of polybrene, followed by centrifugation at 1,500 × *g* for 1 h at RT, and resuspended in 250 µL primary B cell media supplemented with 5 µg/mL LPS (Sigma)

overnight. Cells were treated with 10 µg/mL anti-CD40 (BioLegend) or 25 ng/mL murine IL-21 (PeproTech), alone or in combinations, as indicated. For *ex vivo* infection, primary B cells were plated at a cell density of 1×10^6 cells/mL, in 200 µL of primary B cell media in each well of a 24-well plate.

At day 6 post puromycin selection, Cas9+ GM12878 cells were seeded at a density of 5×10^5 cells/mL in RPMI with 10% fetal bovine serum (FBS; Gibco) in 12 well plates. LCLs were mock stimulated with PBS or with IL-21 (BioLegend, 100 ng/mL in PBS). LCLs were re-seeded in fresh culture medium supplemented with IL-21 every 2 days and assayed by FACS at the end of 6 days.

Limiting dilution analysis of latency and reactivation

To determine the frequency of cells harboring the viral genome as an indicator of latency, single-cell suspensions were analyzed by single-copy-nested PCR as previously described (119). To determine the frequency of cells harboring latent virus capable of reactivation upon explant, single-cell suspensions were plated in 12 serial twofold dilutions on a monolayer of MEF cells prepared from C57BL/6 mice and scored for CPE 3 weeks after plating. Parallel samples were mechanically disrupted using a Mini-Bead-Beater prior to plating on the monolayer of MEFs to release preformed virus and score for preformed infectious virus (119).

Immunoblotting

Total protein lysate was harvested in lysis buffer [150 mM sodium chloride, 1.0% IGEPAL CA-630, 0.5% sodium deoxycholate, 0.1% sodium dodecyl sulfate, 50 mM Tris (pH 8.0)] supplemented with a protease inhibitor cocktail (Sigma, St. Louis, MO). Proteins were separated on 4%–20% SDS-PAGE gels and transferred to a polyvinylidene fluoride membrane. Antibodies against STAT3 (clone K-15; Santa Cruz Biotechnology, Dallas, TX) and α-tubulin (clone B-5-1-2; Sigma) were detected using secondary anti-mouse (Rockland, Limerick, PA) or secondary anti-rabbit (Invitrogen, Grand Island, NY) antibodies by immunoblot analysis with an Odyssey Imager (Li-COR Biosciences, Lincoln, NE).

Flow cytometry

For the analysis of murine B cells and T cells, 2×10^6 splenocytes were resuspended in 50 µL of FACS buffer (PBS with 2% FBS) and blocked with TruStain fcX (clone 93; BioLegend, San Diego, CA). The cells were washed and stained to identify B cell subsets with fluorophore-conjugated antibodies against CD45.2 (clone 104), CD19 (clone 6D5), B220 (clone RA3-682), CD138 (clone 281-2), CD95 (clone 15A7), CD21 (clone 7E9), CD23 (clone B3B4), CXCR4 (clone L276F12), CD86 (clone GL-1), and CD3 (clone 17A2) or biotinylated antibody against GL7 (clone GL-7) that was detected using secondary streptavidin-conjugated allophycocyanin-cyanin7. T cell subsets were identified with antibodies against CD4 (clone GK1.5), CD8 (clone 53-6.7), CD44 (clone IM7), CD127 (clone A7R34), KLRG1 (clone 2F1/KLRG1), TCRβ (clone H57-597). H-2K(b)-p79 MHC-peptide complex was provided as biotinylated monomers by the NIH tetramer core facility and reconstituted with streptavidin-conjugated allophycocyanin. For STAT3-Y705 phosphorylation detection, cells were blocked with TruStain fcX before staining for surface markers. Following fixation and permeabilization with Fixation/Permeabilization Kit (BD Biosciences, San Jose, CA), cells were permeabilized a second time in ice cold 100% methanol for 20 min. Cells were then stained with PE anti-STAT3 Phospho (Tyr705) antibody (Biolegend). For sorting, splenocytes were first enriched for B cells by depletion of non-B cells with magnetic microbeads (Pan B Cell Isolation Kit; Stemcell, Vancouver, BC, Canada) and then sorted using antibodies described above on a FACSAria III sorter (BD Biosciences) or MoFlo sorter (Beckman Coulter, Indianapolis, IN) into cold FACS buffer. All antibodies were purchased from BioLegend, Invitrogen, or BD Biosciences. The data were collected using a CytoFLEX flow cytometer (Beckman Coulter) and analyzed

using FlowJo v10.8.1 (Treestar Inc., Ashland, OR). Dead cells were excluded based on Alexa Fluor 700 NHS Ester uptake. Doublets were excluded through forward scatter-height by forward scatter-area parameters.

For the analysis of EBV+ LCLs, cells were washed once with FACS buffer (2% FBS in PBS) and then stained with APC conjugated anti-CD23 (5 uL per samples) for 30 min at room temperature. Stained cells were washed twice with FACS buffer and analyzed by flow cytometry on a BD FACSCalibur instrument.

Enzyme-linked immunosorbent assay

To measure total IgG levels and antibody specificity in the serum, plates were coated with either 2 µg/mL of donkey anti-mouse IgG (Affinipure; Jackson ImmunoResearch Laboratories, West Grove, PA), carbonate buffer (0.0875 M Na_2CO_3, 0.0125 M HCO_3, pH 9.2) or 0.5% paraformaldehyde-fixed viral antigen-carbonate buffer and incubated overnight at 4°C. Coated plates were washed in PBS with 0.05% Tween 20 (PBS-T) and blocked in 3% milk-PBS-T prior to incubation with serial dilutions of serum or the mouse IgG standard (Invitrogen, Jackson ImmunoResearch) in 1% milk-PBS-T for 2 h at RT. IgG was detected by the use of horseradish peroxidase-conjugated donkey anti-mouse IgG (Jackson ImmunoResearch), SureBlue TMB (SeraCare, Milford, PA), and stop solution, and absorbance at 450 nm was read on FluoStar Omega (BMT Labtech, Cary, NC).

Neutralization assay

Neutralization was tested by means of a plaque reduction neutralization test adapted from reference (54). Briefly, threefold serum dilutions, starting from an initial concentration of 1:80 in Dulbecco's modified Eagle medium (DMEM) supplemented with 10% FBS, 100 U/mL penicillin, 100 µg/mL streptomycin, and 2 mM L-glutamine, were incubated with 150 PFU of MHV68 on ice for 1 h. The virus/serum mixture was then added to a sub-confluent BHK21 monolayer (4×10^4 cells/well) plated the previous day in a 24-well plate, in triplicate. As a control, three wells received no-serum-added virus. Plates were rocked every 15 min for 1 h at 37°C. Infected cells were overlaid with 1.5% methyl cellulose solution in DMEM containing 2.5% FBS and incubated at 37°C for 3–4 days. Methylcellulose media was then aspirated, and cell monolayers were stained with a solution of crystal violet (0.1%) in formalin to facilitate identification and quantification of plaques. Percent neutralization was determined by comparison of the number of plaques in experimental wells compared to no-serum-added control wells, and each data point was the average of three wells.

Immunofluorescence

For confocal microscopy of frozen spleen sections, spleens were removed at the indicated day post-infection, fixed in periodate-lysine-paraformaldehyde fixative for 48 h, and then moved to 30% sucrose/PBS solution for 24 h. Tissues were embedded in optimal-cutting-temperature medium (Electron Microscopy Sciences) and frozen in dry-ice-cooled isopentane. 16-µm sections were cut on a Leica cryostat (Leica Microsystems, Buffalo Grove, IL). Sections were blocked with 5% goat, donkey, bovine, rat, or rabbit serum and then stained with a combination of the following Abs: ERTR7 (Abcam, Boston, MA), B220 (clone RA3-6B2, Biolegend), GL7 (clone GL-7, Thermo Fisher Scientific), and CD21/35 (clone eBio4E3, eBioscience, San Diego, CA). Sections were incubated with secondary antibodies as needed and for controls, and images were acquired on a Leica SP8 or Stellaris Confocal microscope. To increase staining intensity of MHV68, spleens were stained with anti-GFP Ab (EPR14104, Abcam) and goat anti-chicken Alexa Fluor 488 (ThermoFisher Scientific, Waltham, MA). Images were processed and analyzed using Imaris software 8.0 (Oxford Instruments). Where indicated, the spots function of Imaris was used to identify and create spots for MHV68+ cells. Spots were masked on TdTomato expression inside the spot to reveal MHV68+ tdTomato+ cells, referred to as "gated."

RNA-sequencing

A quantity of 5×10^4 cells sorted on the markers of interest by flow cytometry were spun down, resuspended in 50 µL of TRIzol, and stored at −80°C. GENEWIZ (South Plainfield, NJ) performed RNA extraction, quality control, library preparation, and Illumina sequencing.

The custom reference genome allowing quantification of both viral and host expression used in this alignment ("mm10_MHV68YFP_Krug") consisted of the mouse reference (mm10/Apr. 2019/GRCm38) with a modified MHV68 sequence added as an additional pseudochromosome. This viral genome was prepared from the annotated herpesvirus genome (NCBI reference U97553.2) with the addition of a CMV-driven histone 2b-YFP fusion gene locus found in the recombinant MHV68-H2bYFP. The custom gene annotations used for gene expression quantification consisted of a concatenation of the mm10 GENCODE annotation version M21 [99] and annotations of the MHV68 genome. The first annotation ("mm10_MHV68YFP_Krug_Ov") measures expression using complete viral ORF annotations, including those regions that overlap. In the second annotation ("mm10_MHV68YFP_Krug_NoOv"), overlapping regions of the viral ORFs were removed to create a minimal, non-overlapping annotation. This second annotation was used to make conservative estimates of the expression of individual viral genes reported here.

Raw sequencing files were aligned and counted using the CCR Collaborative Bioinformatics Resource in-house pipeline (https://github.com/CCBR/Pipeliner). Briefly, reads were trimmed of low-quality bases, and adapter sequences were removed using Cutadapt v1.18 (http://gensoft.pasteur.fr/docs/cutadapt/1.18). Mapping of reads to the custom reference hybrid genome described below was performed using STAR v2.7.0f in two-pass mode (120, 121). Then, RSEM v1.3.0 was used to quantify gene-level expression (122), with quantile normalization and differential expression of genes analysis performed using limma-voom v3.38.3 (123). The data discussed in this publication, the custom genome reference FASTA, and both annotation GTFs have been deposited in NCBI's Gene Expression Omnibus and are accessible through GEO Series accession GSE227765.

Bioinformatics analysis and visualization

Data analysis and visualization were performed in the NIH Integrated Analysis Portal (NIDAP) using R programs developed on Foundry (Palantir Technologies) for normalization, differential expression analysis, GSEA, and visualization. First, raw counts were imported and transformed to counts per million (CPM) and filtered to retain genes that had at least two samples with non-zero CPM counts in at least one group. Next, quantile normalization and batch correction across samples were used to account for factors that would prevent direct comparisons between samples. Heatmaps were created using the quantile-normalized, batch-corrected RNA-seq data. A principal component analysis demonstrating the within- and between-group variance in expression after dimensionality reduction was generated using NIDAP. Differential expression of genes analysis utilized $\log_2$-CPM transformed raw counts, implemented with the Limma Voom R package. Volcano plots were created from DEG analysis of each comparison highlighting significant fold changes ($\log_2$ fold change) >1 or <−1, with a significant *P* value (adj *P* value <0.05). GSEA in NIDAP used the Limma Voom calculated *t*-statistic ranking to test comparisons against the Broad Institute GSEA hallmark-curated gene sets. Bubble plots generated to display GSEA outputs were generated using SRPLOT (http://www.bioinformatics.com.cn/plot_basic_gopathway_enrichment_bubbleplot_081_en).

Gene signatures were developed using the Molecular Signature Database [MSigDB, (124)] with GO annotations provided by the Gene Ontology resource (125, 126). Germinal center signature was developed using intersection of the following GO data sets: GO:0002314, GO:0002467, GO:0002636, and GO:0002634, accessed on 15 December 2022. Viral infection signature was developed using intersection of the following GO data sets: Hallmark: MM3877, GO:0016032, GO:0039528, GO:0045071, GO:1903901, and

GO:0002230. Hierarchical clustering heatmaps were generated using Morpheus (https://software.broadinstitute.org/morpheus). Hierarchical clustering for all samples or 350 top variable genes was performed using a one minus pearson correlation metric, with complete linkage. CPM trimmed mean of M (TMM) values for viral ORFs were normalized using a scaling factor generated from median total viral counts of samples within a data set.

Statistical analyses

Data were analyzed using GraphPad Prism software (Prism 8; GraphPad Software, Inc., La Jolla, CA). Significance was evaluated by unpaired two-tailed *t* test, paired *t* test, one-way ANOVA, or paired one-tailed *t* test of the log-transformed frequency values of samples from matched experiments, as noted. Using Poisson distribution analysis, the frequencies of latency establishment and reactivation from latency were determined by the intersection of non-linear regression curves with the line at 63.2%.

ACKNOWLEDGMENTS

We thank the laboratories of Robert Yarchoan and Joseph M. Ziegelbauer for sharing critical equipment, as well as flow cytometry cores, animal facilities, and support staff at Stony Brook University and the National Institutes of Health. We also thank Adrianus Van Der Velden, Pawan Kumar, Flaminia Talos, and members of the Krug laboratory for helpful discussion. This work utilized the computational resources of the NIH HPC Biowulf cluster (http://hpc.nih.gov).

This research was supported in part by the Intramural Research Programs of the NIH, the National Cancer Institute (NCI) (C.H.H. and L.T.K.), and the National Institute of Allergy and Infectious Diseases (NIAID) (G.V.S. and H.D.H.). C.H.H., L.T.K., and N.C.R. were supported by NIH NCI RO1AI119079. S.M.O. was supported by a postdoctoral fellowship from Translational Research Institute (TRI) grant TL1 TR003109 through the NIH National Center for Advancing Translational Sciences. Y.L. was supported by a postdoctoral fellowship from Lymphoma Research Foundation. K.M.M. was supported by NIH NIAID R01AI12539, the Recombinant Antibody Production Core [CPRIT RP190507], and the Virginia Harris Cockrell endowment fund. B.E.G. was supported by NIH NIAID AI164709, NIH NCI CA228700, and U01CA275301. J.C.F. was supported by NIH NCI R01CA167065 and NIH NIAID R21AI139580.

AUTHOR AFFILIATIONS

[1]Graduate Program in Genetics, Stony Brook University, Stony Brook, New York, USA
[2]HIV & AIDS Malignancy Branch, National Cancer Institute, NIH, Bethesda, Maryland, USA
[3]Department of Microbiology and Immunology, University of Arkansas for Medical Sciences, Little Rock, Arkansas, USA
[4]Viral Immunity and Pathogenesis Unit, Laboratory of Clinical Immunology and Microbiology, National Institute of Allergy and Infectious Diseases, NIH, Bethesda, Maryland, USA
[5]Division of Infectious Disease, Department of Medicine, Brigham and Women's Hospital, Harvard Medical School, Boston, Massachusetts, USA
[6]CCR Collaborative Bioinformatics Resource, National Cancer Institute, National Institutes of Health, Bethesda, Maryland, USA
[7]Advanced Biomedical Computational Science, Frederick National Laboratory for Cancer Research, Frederick, Maryland, USA
[8]Department of Epigenetics and Molecular Carcinogenesis, The University of Texas MD Anderson Cancer Center, Houston, Texas, USA
[9]Department of Microbiology and Immunology, Renaissance School of Medicine, Stony Brook University, Stony Brook, New York, USA
[10]Harvard Program in Virology, Harvard Medical School, Boston, Massachusetts, USA
[11]Department of Microbiology, Harvard Medical School, Boston, Massachusetts, USA

[12]Broad Institute of Harvard and MIT, Cambridge, Massachusetts, USA

PRESENT ADDRESS

Chad H. Hogan, Institute for Genomic Health, Icahn School of Medicine at Mount Sinai, New York, USA

AUTHOR ORCIDs

Anna K. Grosskopf http://orcid.org/0000-0001-5814-1349
Kevin M. McBride http://orcid.org/0000-0001-9646-152X
Heather D. Hickman http://orcid.org/0000-0003-4168-4894
Laurie T. Krug http://orcid.org/0000-0002-9648-522X

FUNDING

Funder	Grant(s)	Author(s)
HHS | NIH | National Center for Advancing Translational Sciences (NCATS)	TL1 TR003109	Shana M. Owens
HHS | NIH | National Cancer Institute (NCI)	RO1AI119079	Chad H. Hogan
HHS | NIH | NIAID | Division of Intramural Research, National Institute of Allergy and Infectious Diseases (DIR, NIAID)		Glennys V. Reynoso
HHS | NIH | National Cancer Institute (NCI)	Intramural	Laurie T. Krug
Lymphoma Research Foundation (LRF)		Yifei Liao
HHS | NIH | National Cancer Institute (NCI)	Intramural	Thomas J. Meyer
HHS | NIH | National Institute of Allergy and Infectious Diseases (NIAID)	RO1AI119079	Nancy C. Reich
HHS | NIH | National Institute of Allergy and Infectious Diseases (NIAID)	R01AI12539	Kevin M. McBride
HHS | NIH | National Cancer Institute (NCI)	R01CA167065	J. Craig Forrest
HHS | NIH | National Institute of Allergy and Infectious Diseases (NIAID)	R21AI139580	J. Craig Forrest
HHS | NIH | National Institute of Allergy and Infectious Diseases (NIAID)	RO1AI119079	Laurie T. Krug
Cancer Prevention and Research Institute of Texas (CPRIT)	RP190507	Kevin M. McBride
HHS | NIH | National Institute of Allergy and Infectious Diseases (NIAID)	AI164709	Benjamin E. Gewurz
HHS | NIH | National Cancer Institute (NCI)	CA228700	Benjamin E. Gewurz
HHS | NIH | National Cancer Institute (NCI)	U01CA275301	Benjamin E. Gewurz

AUTHOR CONTRIBUTIONS

Chad H. Hogan, Conceptualization, Data curation, Formal analysis, Investigation, Methodology, Project administration, Validation, Visualization, Writing – original draft, Writing – review and editing | Shana M. Owens, Formal analysis, Investigation, Methodology, Validation, Visualization, Writing – review and editing | Glennys V. Reynoso, Investigation, Validation, Visualization | Yifei Liao, Conceptualization, Data curation, Formal analysis, Funding acquisition, Investigation, Methodology, Writing – original draft, Writing – review and editing | Thomas J. Meyer, Data curation, Formal analysis, Investigation, Methodology, Software, Visualization, Writing – original draft, Writing – review and editing | Monika A. Zelazowska, Data curation, Formal analysis, Investigation, Methodology, Software, Visualization, Writing – original draft, Writing – review and editing | Bin Liu, Formal analysis, Investigation, Methodology | Xiaofan Li, Formal analysis,

Investigation, Methodology, Validation, Writing – review and editing | Anna K. Grosskopf, Formal analysis, Validation, Visualization, Writing – review and editing | Camille Khairallah, Conceptualization, Formal analysis, Investigation, Methodology | Varvara Kirillov, Formal analysis, Investigation, Methodology, Resources, Validation | Nancy C. Reich, Conceptualization, Funding acquisition, Investigation, Methodology, Project administration, Resources, Supervision, Writing – review and editing | Brian S. Sheridan, Conceptualization, Formal analysis, Funding acquisition, Investigation, Methodology, Resources, Supervision, Validation, Writing – review and editing | Kevin M. McBride, Conceptualization, Data curation, Formal analysis, Funding acquisition, Investigation, Methodology, Resources, Supervision, Validation, Visualization, Writing – original draft, Writing – review and editing | Benjamin E. Gewurz, Conceptualization, Formal analysis, Funding acquisition, Investigation, Methodology, Resources, Supervision, Visualization, Writing – review and editing | Heather D. Hickman, Conceptualization, Formal analysis, Funding acquisition, Investigation, Methodology, Resources, Supervision, Visualization, Writing – review and editing, Writing – original draft | J. Craig Forrest, Conceptualization, Data curation, Formal analysis, Funding acquisition, Investigation, Methodology, Resources, Supervision, Validation, Visualization, Writing – original draft, Writing – review and editing | Laurie T. Krug, Conceptualization, Data curation, Formal analysis, Funding acquisition, Investigation, Methodology, Project administration, Resources, Supervision, Validation, Visualization, Writing – original draft, Writing – review and editing

DATA AVAILABILITY

Further information and requests for resources and reagents should be directed to and will be fulfilled by the lead contact, Laurie T. Krug (laurie.krug@nih.gov).
Hybrid genome, raw sample reads, and BAM alignments are accessible through GEO Series accession GSE227765. This paper does not report original code. Any additional information required to reanalyze the data reported in this paper is available from the lead contact upon request.

ADDITIONAL FILES

The following material is available online.

Supplemental Material

Fig. S1 (mBio02998-23- S0001.tiff). Infection time course.
Fig. S2 (mBio02998-23- S0002.tiff). tdTomato controls and GC gating.
Fig. S3 (mBio02998-23- S0003.tiff). Viral gene expression in GC B cells.
Fig. S4 (mBio02998-23- S0004.tiff). Immunoglobulin heavy and light chain V gene usage.
Fig. S5 (mBio02998-23- S0005.tiff). GSEA and qRT-PCR analysis of ISGs.
Fig. S6 (mBio02998-23- S0006.tiff). qRT-PCR analysis of B cell genes.
Fig. S7 (mBio02998-23- S0007.tiff). Cytokine stimulation of STAT3 and impact on CD23.
Supplemental Methods and Legends (mBio02998-23- S0008.docx). Supplemental text.
Table S1 (mBio02998-23- S0009.xlsx). Viral gene expression.
Table S2 (mBio02998-23- S0010.xlsx). Identification of genes in clusters.

REFERENCES

1. Soldan SS, Lieberman PM. 2023. Epstein–barr virus and multiple sclerosis. Nat Rev Microbiol 21:51–64. https://doi.org/10.1038/s41579-022-00770-5
2. Farrell PJ. 2019. Epstein–barr virus and cancer. Annual Review of Pathology: Mechanisms of Disease. https://doi.org/10.1146/annurev-pathmechdis
3. Broussard G, Damania B. 2019. KSHV: immune modulation and Immunotherapy. Front Immunol 10:3084. https://doi.org/10.3389/fimmu.2019.03084
4. Cesarman E, Damania B, Krown SE, Martin J, Bower M, Whitby D. 2019. Kaposi sarcoma. Nat Rev Dis Primers 5:9. https://doi.org/10.1038/s41572-019-0060-9
5. Wang Y, Tibbetts SA, Krug LT. 2021. Conquering the host: determinants of pathogenesis learned from murine gammaherpesvirus 68. Annu Rev Virol 8:349–371. https://doi.org/10.1146/annurev-virology-011921-082615
6. Li X, Bhaduri-McIntosh S. 2016. A central role for STAT3 in gammaherpesvirus-life cycle and -diseases. Front Microbiol 7:1052. https://doi.org/10.3389/fmicb.2016.01052

7. Forbes LR, Milner J, Haddad E. 2016. Signal transducer and activator of transcription 3: a year in review. Curr Opin Hematol 23:23–27. https://doi.org/10.1097/MOH.0000000000000206
8. Hillmer EJ, Zhang H, Li HS, Watowich SS. 2016. STAT3 signaling in immunity. Cytokine Growth Factor Rev 31:1–15. https://doi.org/10.1016/j.cytogfr.2016.05.001
9. El-Tanani M, Al Khatib AO, Aladwan SM, Abuelhana A, McCarron PA, Tambuwala MM. 2022. Importance of STAT3 signalling in cancer, metastasis and therapeutic interventions. Cell Signal 92:110275. https://doi.org/10.1016/j.cellsig.2022.110275
10. Wang H, Man Q, Huo F, Gao X, Lin H, Li S, Wang J, Su F, Cai, L, Shi Y, Liu, B, Bu L. 2022. STAT3 pathway in cancers: past, present, and future. MedComm 3:e124: https://doi.org/10.1002/mco2.124
11. Johnson DE, O'Keefe RA, Grandis JR. 2018. Targeting the IL-6/JAK/STAT3 signalling axis in cancer. Nat Rev Clin Oncol 15:234–248. https://doi.org/10.1038/nrclinonc.2018.8
12. Rébé C, Ghiringhelli F. 2019. STAT3, a master regulator of anti-tumor immune response. Cancers (Basel) 11:1280. https://doi.org/10.3390/cancers11091280
13. Lo A-F, Dawson CW, Lung HL, Wong K-L, Young LS. 2021. The role of EBV-encoded LMP1 in the NPC tumor microenvironment: from function to therapy. Front Oncol 11:640207. https://doi.org/10.3389/fonc.2021.640207
14. Lavorgna A, Harhaj EW. 2012. EBV LMP1: new and shared pathways to NF-kappaB activation. Proc Natl Acad Sci U S A 109:2188–2189. https://doi.org/10.1073/pnas.1121357109
15. Li W, Okabe A, Usui G, Fukuyo M, Matsusaka K, Rahmutulla B, Mano Y, Hoshii T, Funata S, Hiura N, Fukayama M, Tan P, Ushiku T, Kaneda A. 2021. Activation of EHF via STAT3 phosphorylation by LMP2A in Epstein - Barr virus–positive gastric cancer. Cancer Sci. 112:3349–3362. https://doi.org/10.1111/cas.14978
16. Incrocci R, Barse L, Stone A, Vagvala S, Montesano M, Subramaniam V, Swanson-Mungerson M. 2017. Epstein-Barr virus latent membrane protein 2A (LMP2A) enhances IL-10 production through the activation of bruton's tyrosine kinase and STAT3. Virology 500:96-102.
17. Jochum S, Moosmann A, Lang S, Hammerschmidt W, Zeidler R. 2012. The EBV Immunoevasins vIL-10 and BNLF2A protect newly infected B cells from immune recognition and elimination. PLoS Pathog 8:e1002704. https://doi.org/10.1371/journal.ppat.1002704
18. Yoon SI, Jones BC, Logsdon NJ, Harris BD, Kuruganti S, Walter MR. 2012. Epstein-barr virus IL-10 engages IL-10R1 by a two-step mechanism leading to altered signaling properties. J Biol Chem 287:26586–26595. https://doi.org/10.1074/jbc.M112.376707
19. Rivera-Soto R, Dissinger NJ, Damania B. 2020. Kaposi's sarcoma-associated herpesvirus viral interleukin-6 signaling upregulates integrin Beta3 levels and is dependent on STAT3. J Virol 94:e01384-19. https://doi.org/10.1128/JVI.01384-19
20. Li W, Wang Q, Qi X, Guo Y, Lu H, Chen Y, Lu Z, Yan Q, Zhu X, Jung JU, Tosato G, Gao SJ, Lu C. 2020. Viral interleukin-6 encoded by an oncogenic virus promotes angiogenesis and cellular transformation by enhancing STAT3-mediated epigenetic silencing of caveolin 1. Oncogene 39:4603–4618. https://doi.org/10.1038/s41388-020-1317-1
21. Liu M. 2010. P38 and STAT3 activation by vGPCR in KSHV-infected cells. Virus Adapt Treat:103. https://doi.org/10.2147/VAAT.S13434
22. Collins CM, Speck SH. 2012. Tracking murine gammaherpesvirus 68 infection of germinal center B cells *in vivo*. PLoS One 7:e33230. https://doi.org/10.1371/journal.pone.0033230
23. Collins CM, Speck SH. 2014. Expansion of murine gammaherpesvirus latently infected B cells requires T follicular help. PLoS Pathog 10:e1004106. https://doi.org/10.1371/journal.ppat.1004106
24. Collins CM, Speck SH. 2015. Interleukin 21 signaling in B cells is required for efficient establishment of murine gammaherpesvirus latency. PLoS Pathog 11:e1004831. https://doi.org/10.1371/journal.ppat.1004831
25. Cieniewicz B, Santana AL, Minkah N, Krug LT. 2016. Interplay of murine gammaherpesvirus 68 with NF-kappaB signaling of the host. Front Microbiol 7:1202. https://doi.org/10.3389/fmicb.2016.01202
26. Kim I-J, Flaño E, Woodland DL, Lund FE, Randall TD, Blackman MA. 2003. Maintenance of long term gamma-herpesvirus B cell latency is dependent on CD40-mediated development of memory B cells. J Immunol 171:886–892. https://doi.org/10.4049/jimmunol.171.2.886
27. Cieniewicz B, Kirillov V, Daher I, Li X, Oldenburg DG, Dong Q, Bettke JA, Marcu KB, Krug LT. 2022. IKKa-mediated noncanonical NF-K B signaling is required to support murine gammaherpesvirus 68 latency *in vivo*. J Virol 96:e0002722. https://doi.org/10.1128/jvi.00027-22
28. Young C, Brink R. 2021. The unique biology of germinal center B cells. Immunity 54:1652–1664. https://doi.org/10.1016/j.immuni.2021.07.015
29. Victora GD, Nussenzweig MC. 2022. Germinal centers. Annu Rev Immunol 40:413–442. https://doi.org/10.1146/annurev-immunol-120419-022408
30. Thorley-LawsonDA. 2015. Epstein Barr virus volume 1: one herpes virus: many diseases, p 151–209. In Münz C (ed), EBV persistence—introducing the virus. Springer International Publishing, Cham.
31. Hassman LM, Ellison TJ, Kedes DH. 2011. KSHV Infects a subset of human tonsillar B cells, driving proliferation and plasmablast differentiation. J Clin Invest 121:752–768. https://doi.org/10.1172/JCI44185
32. Knowlton ER, Rappocciolo G, Piazza P, Lepone LM, Nadgir SV, Bullotta A, Berendam SJ, Li J, Reinhart TA, Jenkins FJ, Rinaldo CR, Racaniello V. 2014. Human herpesvirus 8 induces polyfunctional B lymphocytes that drive Kaposi's sarcoma. mBio 5. https://doi.org/10.1128/mBio.01277-14
33. Aalam F, Nabiee R, Castano JR, Totonchy J, Tarakanova VL. 2020. Analysis of KSHV B lymphocyte lineage tropism in human tonsil reveals efficient infection of CD138+ plasma cells. PLoS Pathog 16:e1008968. https://doi.org/10.1371/journal.ppat.1008968
34. Zelazowska MA, Dong Q, Plummer JB, Zhong Y, Liu B, Krug LT, McBride KM. 2020. Gammaherpesvirus-infected germinal center cells express a distinct immunoglobulin repertoire. Life Sci Alliance 3:e201900526. https://doi.org/10.26508/lsa.201900526
35. Pei Y, Lewis AE, Robertson ES. 2017. Current Progress in EBV-Associated B-Cell Lymphomas, p 57-74. In Cai Q, Yuan Z, Lan K (ed), Infectious Agents Associated Cancers: epidemiology and molecular biology. Springer, Singapore.
36. Cesarman E, Chadburn A, Rubinstein PG. 2022. KSHV/HHV8-mediated hematologic diseases. Blood 139:1013–1025. https://doi.org/10.1182/blood.2020005470
37. Siegel AM, Rangaswamy US, Napier RJ, Speck SH. 2010. Blimp-1-dependent plasma cell differentiation is required for efficient maintenance of murine gammaherpesvirus latency and antiviral antibody responses. J Virol 84:674–685. https://doi.org/10.1128/JVI.01306-09
38. Siegel AM, Herskowitz JH, Speck SH. 2008. The MHV68 M2 protein drives IL-10 dependent B cell proliferation and differentiation. PLoS Pathog 4:e1000039. https://doi.org/10.1371/journal.ppat.1000039
39. Rangaswamy US, Speck SH. 2014. Murine gammaherpesvirus M2 protein induction of IRF4 via the NFAT pathway leads to IL-10 expression in B cells. PLoS Pathog 10:e1003858. https://doi.org/10.1371/journal.ppat.1003858
40. Terrell S, Speck SH. 2017. Murine gammaherpesvirus M2 antigen modulates splenic B cell activation and terminal differentiation *in vivo*. PLoS Pathog 13:e1006543. https://doi.org/10.1371/journal.ppat.1006543
41. Foreman H-CC, Armstrong J, Santana AL, Krug LT, Reich NC. 2017. The replication and transcription activator of murine gammaherpesvirus 68 cooperatively enhances cytokine-activated, STAT3-mediated gene expression. J Biol Chem 292:16257–16266. https://doi.org/10.1074/jbc.M117.786970
42. Reddy SS, Foreman H-C, Sioux TO, Park GH, Poli V, Reich NC, Krug LT. 2016. Ablation of STAT3 in the B cell compartment restricts gammaherpesvirus latency *in vivo*. mBio 7:e00723-16. https://doi.org/10.1128/mBio.00723-16
43. Fornek JL, Tygrett LT, Waldschmidt TJ, Poli V, Rickert RC, Kansas GS. 2006. Critical role for STAT3 in T-dependent terminal differentiation of IgG B cells. Blood 107:1085–1091. https://doi.org/10.1182/blood-2005-07-2871
44. Alonzi T, Maritano D, Gorgoni B, Rizzuto G, Libert C, Poli V. 2001. Essential role of STAT3 in the control of the acute-phase response as revealed by inducible gene inactivation. Mol Cell Biol 21:1621–1632. https://doi.org/10.1128/MCB.21.5.1621-1632.2001
45. Moh A, Iwamoto Y, Chai G-X, Zhang SS-M, Kano A, Yang DD, Zhang W, Wang J, Jacoby JJ, Gao B, Flavell RA, Fu X-Y. 2007. Role of STAT3 in liver regeneration: survival, DNA synthesis, inflammatory reaction and liver

mass recovery. Lab Invest 87:1018–1028. https://doi.org/10.1038/labinvest.3700630
46. Santarelli R, Gonnella R, Di Giovenale G, Cuomo L, Capobianchi A, Granato M, Gentile G, Faggioni A, Cirone M. 2014. STAT3 activation by KSHV correlates with IL-10, IL-6 and IL-23 release and an autophagic block in dendritic cells. Sci Rep 4:4241. https://doi.org/10.1038/srep04241
47. Daigle D, Megyola C, El-Guindy A, Gradoville L, Tuck D, Miller G, Bhaduri-McIntosh S. 2010. Upregulation of STAT3 marks Burkitt lymphoma cells refractory to Epstein-Barr virus lytic cycle induction by HDAC inhibitors. J Virol 84:993–1004. https://doi.org/10.1128/JVI.01745-09
48. Cousins E, Nicholas J. 2013. Role of human herpesvirus 8 interleukin-6-activated gp130 signal transducer in primary effusion lymphoma cell growth and viability. J Virol 87:10816–10827. https://doi.org/10.1128/JVI.02047-13
49. Punjabi AS, Carroll PA, Chen L, Lagunoff M. 2007. Persistent activation of STAT3 by latent Kaposi's sarcoma-associated herpesvirus infection of endothelial cells. J Virol 81:2449–2458. https://doi.org/10.1128/JVI.01769-06
50. Ding BB, Bi E, Chen H, Yu JJ, Ye BH. 2013. IL-21 and CD40L synergistically promote plasma cell differentiation through upregulation of Blimp-1 in human B cells. J Immunol 190:1827–1836. https://doi.org/10.4049/jimmunol.1201678
51. Diehl SA, Schmidlin H, Nagasawa M, van Haren SD, Kwakkenbos MJ, Yasuda E, Beaumont T, Scheeren FA, Spits H. 2008. STAT3-mediated up-regulation of Blimp1 is coordinated with BCL6 down-regulation to control human plasma cell differentiation. J Immunol 180:4805–4815. https://doi.org/10.4049/jimmunol.180.7.4805
52. Liang X, Collins CM, Mendel JB, Iwakoshi NN, Speck SH, Damania B. 2009. Gammaherpesvirus-driven plasma cell differentiation regulates virus reactivation from latently infected B lymphocytes. PLoS Pathog 5:e1000677. https://doi.org/10.1371/journal.ppat.1000677
53. Stevenson PG, Doherty PC. 1999. Non-antigen-specific B-cell activation following murine gammaherpesvirus infection is CD4 independent *in vitro* but CD4 dependent *in vivo*. J Virol 73:1075–1079. https://doi.org/10.1128/JVI.73.2.1075-1079.1999
54. Stevenson PG, Doherty PC. 1998. Kinetic analysis of the specific host response to a murine gammaherpesvirus. J Virol 72:943–949. https://doi.org/10.1128/JVI.72.2.943-949.1998
55. Barton E, Mandal P, Speck SH. 2011. Pathogenesis and host control of gammaherpesviruses: lessons from the mouse. Annu Rev Immunol 29:351–397. https://doi.org/10.1146/annurev-immunol-072710-081639
56. Krug LT, Collins CM, Gargano LM, Speck SH. 2009. NF-kappaB P50 plays distinct roles in the establishment and control of murine gammaherpesvirus 68 latency. J Virol 83:4732–4748. https://doi.org/10.1128/JVI.00111-09
57. Sagardoy A, Martinez-Ferrandis JI, Roa S, Bunting KL, Aznar MA, Elemento O, Shaknovich R, Fontán L, Fresquet V, Perez-Roger I, Robles EF, De Smedt L, Sagaert X, Melnick A, Martinez-Climent JA. 2013. Downregulation of FOXP1 is required during germinal center B-cell function. Blood 121:4311–4320. https://doi.org/10.1182/blood-2012-10-462846
58. Oliver AM, Martin F, Kearney JF. 1997. Mouse CD38 is down-regulated on germinal center B cells and mature plasma cells. J Immunol 158:1108–1115.
59. Liu L, Flaño E, Usherwood EJ, Surman S, Blackman MA, Woodland DL. 1999. Lytic cycle T cell epitopes are expressed in two distinct phases during MHV-68 infection. J Immunol 163:868–874.
60. Collins CM, Scharer CD, Murphy TJ, Boss JM, Speck SH, Dittmer DP. 2020. Murine gammaherpesvirus infection is SKEWED toward Iglambda+ B cells expressing a specific heavy chain V-segment. PLoS Pathog 16:e1008438. https://doi.org/10.1371/journal.ppat.1008438
61. Burton EM, Gewurz BE, Goodrum F. 2022. Epstein-Barr virus oncoprotein-driven B cell metabolism remodeling. PLoS Pathog 18:e1010254. https://doi.org/10.1371/journal.ppat.1010254
62. Liang X, Shin YC, Means RE, Jung JU. 2004. Inhibition of interferon-mediated antiviral activity by murine gammaherpesvirus 68 latency-associated M2 protein. J Virol 78:12416–12427. https://doi.org/10.1128/JVI.78.22.12416-12427.2004
63. Hwang S, Kim KS, Flano E, Wu TT, Tong LM, Park AN, Song MJ, Sanchez DJ, O'Connell RM, Cheng G, Sun R. 2009. Conserved herpesviral kinase promotes viral persistence by inhibiting the IRF-3-mediated type I interferon response. Cell Host Microbe 5:166–178. https://doi.org/10.1016/j.chom.2008.12.013
64. Leang RS, Wu T-T, Hwang S, Liang LT, Tong L, Truong JT, Sun R, Glaunsinger BA. 2011. The anti-interferon activity of conserved viral dUTPase ORF54 is essential for an effective MHV-68 infection. PLoS Pathog 7:e1002292. https://doi.org/10.1371/journal.ppat.1002292
65. Wood BM, Mboko WP, Mounce BC, Tarakanova VL. 2013. Mouse gammaherpesvirus-68 infection acts as a rheostat to set the level of type I interferon signaling in primary macrophages. Virology 443:123–133. https://doi.org/10.1016/j.virol.2013.04.036
66. Kang HR, Cheong WC, Park JE, Ryu S, Cho HJ, Youn H, Ahn JH, Song MJ. 2014. Murine gammaherpesvirus 68 encoding open reading frame 11 targets TANK binding kinase 1 to negatively regulate the host type I interferon response. J Virol 88:6832–6846. https://doi.org/10.1128/JVI.03460-13
67. Sun C, Schattgen SA, Pisitkun P, Jorgensen JP, Hilterbrand AT, Wang LJ, West JA, Hansen K, Horan KA, Jakobsen MR, O'Hare P, Adler H, Sun R, Ploegh HL, Damania B, Upton JW, Fitzgerald KA, Paludan SR. 2015. Evasion of innate cytosolic DNA sensing by a gammaherpesvirus facilitates establishment of latent infection. J Immunol 194:1819–1831. https://doi.org/10.4049/jimmunol.1402495
68. Lu L, Zhu F, Zhang M, Li Y, Drennan AC, Kimpara S, Rumball I, Selzer C, Cameron H, Kellicut A, Kelm A, Wang F, Waldmann TA, Rui L. 2018. Gene regulation and suppression of type I interferon signaling by STAT3 in diffuse large B cell lymphoma. Proc Natl Acad Sci U S A 115:E498–E505. https://doi.org/10.1073/pnas.1715118115
69. Wang H, Yuan M, Wang S, Zhang L, Zhang R, Zou X, Wang X, Chen D, Wu Z. 2019. STAT3 regulates the type I IFN-mediated antiviral response by interfering with the nuclear entry of STAT1. Int J Mol Sci 20:4870. https://doi.org/10.3390/ijms20194870
70. Tsai MH, Pai LM, Lee CK. 2019. Fine-tuning of type I interferon response by STAT3. Front Immunol 10:1448. https://doi.org/10.3389/fimmu.2019.01448
71. Saeland S, Duvert V, Moreau I, Banchereau J. 1993. Human B cell precursors proliferate and express CD23 after CD40 ligation. J Exp Med 178:113–120. https://doi.org/10.1084/jem.178.1.113
72. Liu YJ, Cairns JA, Holder MJ, Abbot SD, Jansen KU, Bonnefoy JY, Gordon J, MacLennan IC. 1991. Recombinant 25-kDa CD23 and interleukin 1 alpha promote the survival of germinal center B cells: evidence for bifurcation in the development of centrocytes rescued from apoptosis. Eur J Immunol 21:1107–1114. https://doi.org/10.1002/eji.1830210504
73. Hibbert RG, Teriete P, Grundy GJ, Beavil RL, Reljic R, Holers VM, Hannan JP, Sutton BJ, Gould HJ, McDonnell JM. 2005. The structure of human CD23 and its interactions with IgE and CD21. J Exp Med 202:751–760. https://doi.org/10.1084/jem.20050811
74. Zotos D, Coquet JM, Zhang Y, Light A, D'Costa K, Kallies A, Corcoran LM, Godfrey DI, Toellner KM, Smyth MJ, Nutt SL, Tarlinton DM. 2010. IL-21 regulates germinal center B cell differentiation and proliferation through a B cell-intrinsic mechanism. J Exp Med 207:365–378. https://doi.org/10.1084/jem.20091777
75. Zotos D, Quast I, Li-Wai-Suen CSN, McKenzie CI, Robinson MJ, Kan A, Smyth GK, Hodgkin PD, Tarlinton DM. 2021. The concerted change in the distribution of cell cycle phases and zone composition in germinal centers is regulated by IL-21. Nat Commun 12:7160. https://doi.org/10.1038/s41467-021-27477-0
76. Ozaki K, Spolski R, Ettinger R, Kim H-P, Wang G, Qi C-F, Hwu P, Shaffer DJ, Akilesh S, Roopenian DC, Morse HC, Lipsky PE, Leonard WJ. 2004. Regulation of B cell differentiation and plasma cell generation by IL-21, a novel inducer of Blimp-1 and Bcl-6. J Immunol 173:5361–5371. https://doi.org/10.4049/jimmunol.173.9.5361
77. Maliszewski CR, Grabstein K, Fanslow WC, Armitage R, Spriggs MK, Sato TA. 1993. Recombinant CD40 ligand stimulation of murine B cell growth and differentiation: cooperative effects of cytokines. Eur J Immunol 23:1044–1049. https://doi.org/10.1002/eji.1830230510
78. Thorley-Lawson DA, Mann KP. 1985. Early events in Epstein-Barr virus infection provide a model for B cell activation. J Exp Med 162:45–59. https://doi.org/10.1084/jem.162.1.45

79. Ding C, Chen X, Dascani P, Hu X, Bolli R, Zhang H-G, Mcleish KR, Yan J. 2016. STAT3 signaling in B cells is critical for germinal center maintenance and contributes to the pathogenesis of murine models of lupus. J Immunol 196:4477–4486. https://doi.org/10.4049/jimmunol.1502043
80. Fike AJ, Chodisetti SB, Wright NE, Bricker KN, Domeier PP, Maienschein-Cline M, Rosenfeld AM, Luckenbill SA, Weber JL, Choi NM, Luning Prak ET, Mandal M, Clark MR, Rahman ZSM. 2023. STAT3 signaling in B cells controls germinal center zone organization and recycling. Cell Rep 42:112512. https://doi.org/10.1016/j.celrep.2023.112512
81. Herskowitz JH, Jacoby MA, Speck SH. 2005. The murine gammaherpesvirus 68 M2 gene is required for efficient reactivation from latently infected B cells. J Virol 79:2261–2273. https://doi.org/10.1128/JVI.79.4.2261-2273.2005
82. Owens SM, Oldenburg DG, White DW, Forrest JC. 2020. Deletion of murine gammaherpesvirus gene M2 in activation-induced cytidine deaminase-expressing B cells impairs host colonization and viral reactivation. J Virol 95:e01933-20. https://doi.org/10.1128/JVI.01933-20
83. Saraiva M, O'Garra A. 2010. The regulation of IL-10 production by immune cells. Nat Rev Immunol 10:170–181. https://doi.org/10.1038/nri2711
84. Dominguez-Sola D, Victora GD, Ying CY, Phan RT, Saito M, Nussenzweig MC, Dalla-Favera R. 2012. The proto-oncogene MYC is required for selection in the germinal center and cyclic reentry. Nat Immunol 13:1083–1091. https://doi.org/10.1038/ni.2428
85. Calado DP, Sasaki Y, Godinho SA, Pellerin A, Köchert K, Sleckman BP, de Alborán IM, Janz M, Rodig S, Rajewsky K. 2012. The cell-cycle regulator c-Myc is essential for the formation and maintenance of germinal centers. Nat Immunol 13:1092–1100. https://doi.org/10.1038/ni.2418
86. Shirogane T, Fukada T, Muller JM, Shima DT, Hibi M, Hirano T. 1999. Synergistic roles for Pim-1 and c-Myc in STAT3-mediated cell cycle progression and Antiapoptosis. Immunity 11:709–719. https://doi.org/10.1016/s1074-7613(00)80145-4
87. Kiuchi N, Nakajima K, Ichiba M, Fukada T, Narimatsu M, Mizuno K, Hibi M, Hirano T. 1999. STAT3 is required for the gp130-mediated full activation of the c-Myc gene. J Exp Med 189:63–73. https://doi.org/10.1084/jem.189.1.63
88. Liu SY, Sanchez DJ, Aliyari R, Lu S, Cheng G. 2012. Systematic identification of type I and type II interferon-induced antiviral factors. Proc Natl Acad Sci U S A 109:4239–4244. https://doi.org/10.1073/pnas.1114981109
89. Schwerk J, Kemper L, Bussey KA, Lienenklaus S, Weiss S, Čičin-Šain L, Kröger A, Kalinke U, Collins CM, Speck SH, Messerle M, Wirth D, Brinkmann MM, Hauser H, Köster M. 2022. Type I interferon signaling controls gammaherpesvirus latency *in vivo*. Pathogens 11:1554. https://doi.org/10.3390/pathogens11121554
90. Lee KS, Groshong SD, Cool CD, Kleinschmidt-DeMasters BK, van Dyk LF. 2009. Murine gammaherpesvirus 68 infection of IFNgamma unresponsive mice: a small animal model for gammaherpesvirus-associated B-cell lymphoproliferative disease. Cancer Res 69:5481–5489. https://doi.org/10.1158/0008-5472.CAN-09-0291
91. Jondle CN, Tarakanova VL. 2020. Innate immunity and alpha/gammaherpesviruses: first impressions last a lifetime. Curr Opin Virol 44:81–89. https://doi.org/10.1016/j.coviro.2020.07.002
92. Johnson KE, Aurubin CA, Jondle CN, Lange PT, Tarakanova VL. 2020. Interferon regulatory factor 7 attenuates chronic gammaherpesvirus infection. J Virol 94:e01554-20. https://doi.org/10.1128/JVI.01554-20
93. Mboko WP, Rekow MM, Ledwith MP, Lange PT, Schmitz KE, Anderson S, Tarakanova VL, Jung JU. 2017. Interferon regulatory factor 1 and type I interferon cooperate to control acute gammaherpesvirus infection. J Virol 91. https://doi.org/10.1128/JVI.01444-16
94. Goodwin MM, Canny S, Steed A, Virgin HW. 2010. Murine gammaherpesvirus 68 has evolved gamma interferon and STAT1-repressible promoters for the lytic switch gene 50. J Virol 84:3711–3717. https://doi.org/10.1128/JVI.02099-09
95. Sylvester PA, Jondle CN, Stoltz KP, Lanham J, Dittel BN, Tarakanova VL, Jung JU. 2021. Conserved gammaherpesvirus protein kinase counters the antiviral effects of myeloid cell-specific STAT1 expression to promote the establishment of splenic B cell latency. J Virol 95. https://doi.org/10.1128/JVI.00859-21
96. Barton ES, Lutzke ML, Rochford R, Virgin HW. 2005. Alpha/beta Interferons regulate murine gammaherpesvirus latent gene expression and reactivation from latency. J Virol 79:14149–14160. https://doi.org/10.1128/JVI.79.22.14149-14160.2005
97. Zou Z, Meng Z, Ma C, Liang D, Sun R, Lan K. 2017. Guanylate-binding protein 1 inhibits nuclear delivery of Kaposi's sarcoma-associated herpesvirus virions by disrupting formation of actin filament. J Virol 91:e00632-17. https://doi.org/10.1128/JVI.00632-17
98. Ritchie KJ, Hahn CS, Kim KI, Yan M, Rosario D, Li L, de la Torre JC, Zhang D-E. 2004. Role of ISG15 protease UBP43 (USP18) in innate immunity to viral infection. Nat Med 10:1374–1378. https://doi.org/10.1038/nm1133
99. Yang W, Gu Z, Zhang H, Hu H. 2020. To TRIM the immunity: from innate to adaptive immunity. Front Immunol 11:02157. https://doi.org/10.3389/fimmu.2020.02157
100. Goel RR, Nakabo S, Dizon BLP, Urban A, Waldman M, Howard L, Darnell D, Buhaya M, Carmona-Rivera C, Hasni S, Kaplan MJ, Freeman AF, Gupta S. 2021. Lupus-like autoimmunity and increased interferon response in patients with STAT3-deficient hyper-IgE syndrome. J Allergy Clin Immunol 147:746–749. https://doi.org/10.1016/j.jaci.2020.07.024
101. Avery DT, Ma CS, Bryant VL, Santner-Nanan B, Nanan R, Wong M, Fulcher DA, Cook MC, Tangye SG. 2008. STAT3 is required for IL-21-induced secretion of IgE from human naive B cells. Blood 112:1784–1793. https://doi.org/10.1182/blood-2008-02-142745
102. Chang H, Gwack Y, Kingston D, Souvlis J, Liang X, Means RE, Cesarman E, Hutt-Fletcher L, Jung JU. 2005. Activation of CD21 and CD23 gene expression by Kaposi's sarcoma-associated herpesvirus RTA. J Virol 79:4651–4663. https://doi.org/10.1128/JVI.79.8.4651-4663.2005
103. Kempkes B, Pawlita M, Zimber-Strobl U, Eissner G, Laux G, Bornkamm GW. 1995. Epstein-Barr virus nuclear antigen 2-estrogen receptor fusion proteins transactivate viral and cellular genes and interact with RBP-J Kappa in a conditional fashion. Virology 214:675–679. https://doi.org/10.1006/viro.1995.0084
104. Ling PD, Hsieh JJ, Ruf IK, Rawlins DR, Hayward SD. 1994. EBNA-2 upregulation of Epstein-Barr virus latency promoters and the cellular CD23 promoter utilizes a common targeting Intermediate, CBF1. J Virol 68:5375–5383. https://doi.org/10.1128/JVI.68.9.5375-5383.1994
105. Cooper AM, Hobson PS, Jutton MR, Kao MW, Drung B, Schmidt B, Fear DJ, Beavil AJ, McDonnell JM, Sutton BJ, Gould HJ. 2012. Soluble CD23 controls IgE synthesis and homeostasis in human B cells. J Immunol 188:3199–3207. https://doi.org/10.4049/jimmunol.1102689
106. Cordier-Bussat M, Billaud M, Calender A, Lenoir GM. 1993. Epstein-Barr virus (EBV) nuclear-antigen-2-induced up-regulation of CD21 and CD23 molecules is dependent on a permissive cellular context. Int J Cancer 53:153–160. https://doi.org/10.1002/ijc.2910530128
107. Wang F, Gregory C, Sample C, Rowe M, Liebowitz D, Murray R, Rickinson A, Kieff E. 1990. Epstein-Barr virus latent membrane protein (LMP1) and nuclear proteins 2 and 3C are effectors of phenotypic changes in B lymphocytes: EBNA-2 and LMP1 cooperatively induce CD23. J Virol 64:2309–2318. https://doi.org/10.1128/jvi.64.5.2309-2318.1990
108. Wang F, Gregory CD, Rowe M, Rickinson AB, Wang D, Birkenbach M, Kikutani H, Kishimoto T, Kieff E. 1987. Epstein-Barr virus nuclear antigen 2 specifically induces expression of the B-cell activation antigen CD23. Proc Natl Acad Sci U S A 84:3452–3456. https://doi.org/10.1073/pnas.84.10.3452
109. Wang Y, Wang C, Cai X, Mou C, Cui X, Zhang Y, Ge F, Dong H, Hao Y, Cai L, Wu S, Feng C, Chen J, Li J, Xu W, Fan L, Xie W, Tong Y, Gu HF, Wu L. 2020. IL-21 stimulates the expression and activation of cell cycle regulators and promotes cell proliferation in EBV-positive diffuse large B cell lymphoma. Sci Rep 10:12326. https://doi.org/10.1038/s41598-020-69227-0
110. McIntosh MT, Koganti S, Boatwright JL, Li X, Spadaro SV, Brantly AC, Ayers JB, Perez RD, Burton EM, Burgula S, MacCarthy T, Bhaduri-McIntosh S, Wallace N. 2020. STAT3 imparts BRCAness by impairing homologous recombination repair in Epstein-Barr virus-transformed B lymphocytes. PLoS Pathog 16:e1008849. https://doi.org/10.1371/journal.ppat.1008849
111. Wu J, Xu Y, Mo D, Huang P, Sun R, Huang L, Pan S, Xu J, Gao S-J. 2014. Kaposi's sarcoma-associated herpesvirus (KSHV) vIL-6 promotes cell proliferation and migration by upregulating DNMT1 via STAT3 activation. PLoS ONE 9:e93478. https://doi.org/10.1371/journal.pone.0093478
112. Ramalingam D, Ziegelbauer JM. 2017. Viral microRNAs target a gene network, inhibit STAT activation, and suppress interferon responses. Sci Rep 7:40813. https://doi.org/10.1038/srep40813

113. Liu S, Lei Z, Li J, Wang L, Jia R, Liu Z, Jiang C, Gao Y, Liu M, Kuang L, Qian Z, Zhou D, Speck SH, Liang X, Krug LT. 2020. Interleukin 16 contributes to gammaherpesvirus pathogenesis by inhibiting viral reactivation. PLoS Pathog 16:e1008701. https://doi.org/10.1371/journal.ppat.1008701
114. Manzano M, Patil A, Waldrop A, Dave SS, Behdad A, Gottwein E. 2018. Gene essentiality landscape and druggable oncogenic dependencies in herpesviral primary effusion lymphoma. Nat Commun 9:3263. https://doi.org/10.1038/s41467-018-05506-9
115. Collins CM, Boss JM, Speck SH. 2009. Identification of infected B-cell populations by using a recombinant murine gammaherpesvirus 68 expressing a fluorescent protein. J Virol 83:6484–6493. https://doi.org/10.1128/JVI.00297-09
116. Ma Y, Walsh MJ, Bernhardt K, Ashbaugh CW, Trudeau SJ, Ashbaugh IY, Jiang S, Jiang C, Zhao B, Root DE, Doench JG, Gewurz BE. 2017. CRISPR/Cas9 screens reveal Epstein-Barr virus-transformed B cell host dependency factors. Cell Host Microbe 21:580–591. https://doi.org/10.1016/j.chom.2017.04.005
117. Sanson KR, Hanna RE, Hegde M, Donovan KF, Strand C, Sullender ME, Vaimberg EW, Goodale A, Root DE, Piccioni F, Doench JG. 2018. Optimized libraries for CRISPR-Cas9 genetic screens with multiple modalities. Nat Commun 9:5416. https://doi.org/10.1038/s41467-018-07901-8
118. Jiang S, Wang LW, Walsh MJ, Trudeau SJ, Gerdt C, Zhao B, Gewurz BE. 2018. CRISPR/Cas9-mediated genome editing in Epstein-Barr virus-transformed Lymphoblastoid B-cell lines. Curr Protoc Mol Biol 121:31. https://doi.org/10.1002/cpmb.51
119. Weck KE, Kim SS, Virgin HW IV, Speck SH. 1999. B cells regulate murine gammaherpesvirus 68 latency. J Virol 73:4651–4661. https://doi.org/10.1128/JVI.73.6.4651-4661.1999
120. Dobin A, Davis CA, Schlesinger F, Drenkow J, Zaleski C, Jha S, Batut P, Chaisson M, Gingeras TR. 2013. STAR: ultrafast universal RNA-seq aligner. Bioinformatics 29:15–21. https://doi.org/10.1093/bioinformatics/bts635
121. Martin M. 2011. Cutadapt removes adapter sequences from high-throughput sequencing reads. EMBnet j 17:10. https://doi.org/10.14806/ej.17.1.200
122. Li B, Dewey CN. 2011. RSEM: accurate transcript quantification from RNA-seq data with or without a reference genome. BMC Bioinformatics 12:323. https://doi.org/10.1186/1471-2105-12-323
123. Ritchie ME, Phipson B, Wu D, Hu Y, Law CW, Shi W, Smyth GK. 2015. Limma powers differential expression analyses for RNA-sequencing and microarray studies. Nucleic Acids Res 43:e47. https://doi.org/10.1093/nar/gkv007
124. Subramanian A, Tamayo P, Mootha VK, Mukherjee S, Ebert BL, Gillette MA, Paulovich A, Pomeroy SL, Golub TR, Lander ES, Mesirov JP. 2005. Gene set enrichment analysis: a knowledge-based approach for interpreting genome-wide expression profiles. Proc Natl Acad Sci U S A 102:15545–15550. https://doi.org/10.1073/pnas.0506580102
125. Ashburner M, Ball CA, Blake JA, Botstein D, Butler H, Cherry JM, Davis AP, Dolinski K, Dwight SS, Eppig JT, Harris MA, Hill DP, Issel-Tarver L, Kasarskis A, Lewis S, Matese JC, Richardson JE, Ringwald M, Rubin GM, Sherlock G. 2000. Gene ontology: tool for the unification of biology. Nat Genet 25:25–29. https://doi.org/10.1038/75556
126. Gene Ontology C. 2021. The gene ontology resource: enriching a GOld mine. Nucleic Acids Res 49:D325–D334. https://doi.org/10.1093/nar/gkaa1113